ACS APPLIED MATERIALS & INTERFACES

www.acsami.org

Research Article

Engineering Transferrin-Decorated Pullulan-Based Prodrug Nanoparticles for Redox Responsive Paclitaxel Delivery to Metastatic Lung Cancer Cells

Xing Zhao,[#] Haifei Guo,[#] Hriday Bera,[*] Huiyang Jiang, Yang Chen, Xiong Guo, Xidong Tian, Dongmei Cun,[*] and Mingshi Yang[*]

Cite This: *ACS Appl. Mater. Interfaces* 2023, 15, 4441−4457

Read Online

ACCESS | Metrics & More | Article Recommendations | Supporting Information

ABSTRACT: Paclitaxel (PTX) remains a cornerstone in the treatment of locally advanced and metastatic lung cancer. To improve its therapeutic indices against lung cancer, novel redox-sensitive pullulan/PTX-based prodrug NPs (PULL−SS−PTX NPs) were accomplished, which were further surface-decorated with transferrin (TF), a cancer cell-targeting ligand, to afford TF−PULL−SS−PTX NPs. These prodrug NPs (drug content, >37% and average size, 134−163 nm) rapidly dismantled their self-assembled architecture upon exposure to simulated reducing conditions, causing a triggered drug release as compared to the control scaffold (PULL−CC−PTX NPs). These scaffolds also evidenced outstanding colloidal stability, cellular uptake efficiency, and discriminating cytotoxicity between the cancer and healthy cells. Intravenously delivered redox-sensitive NPs exhibited improved tumor-suppressing properties as compared to the control nanovesicles (PULL−CC−PTX NPs) in a B16−F10 melanoma lung metastasis mice model. The targeting efficiency and associated augmented anticancer potentials of TF−PULL−SS−PTX NPs relative to TF-free redox-responsive NPs and Taxol intravenous injection were also established on the transferrin receptor (TFR) overexpressed Lewis lung carcinoma (LLC−luc) cell-bearing mice model. Moreover, the TF-functionalized scaffold displayed a reduced systemic toxicity compared to that of Taxol intravenous injection. Overall, the proposed TF-decorated prodrug NPs could be a promising nanomedicine for intracellular PTX delivery against metastatic lung cancer.

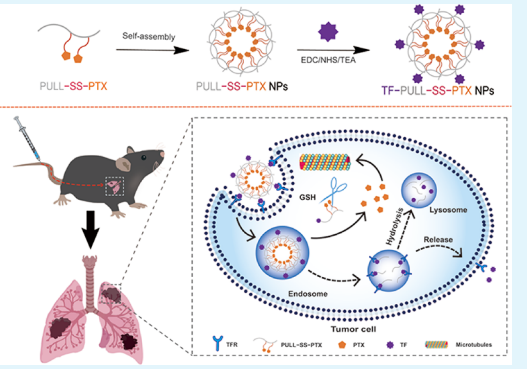

KEYWORDS: *polysaccharide, anticancer drug, conjugation chemistry, glutathione, transferrin receptor, nanomedicine*

1. INTRODUCTION

Lung carcinoma continues to be the leading cause of premature mortality across the globe, accounting for approximately one in five deaths (1.59 million deaths and 19.4% of the total).[1] The vast majority of lung cancer cases are diagnosed at extremely advanced or inoperable metastatic stages, where chemotherapy remains as the primary treatment option.[2] Paclitaxel (PTX) is the cornerstone chemotherapy for the lung cancer treatment and often used in combination with other anticancer drugs.[3] PTX stabilizes microtubules by blocking their depolymerization during the cell division.[4] However, PTX evidences poor inherent solubility and limited oral bioavailability.[5] Taxol, a commercial intravenous PTX formulation constituted with a mixture of dehydrated ethanol and Cremophor EL, is commonly exploited to treat lung cancer. Regrettably, it demonstrates fatal dose-dependent adverse effects owing to their considerably low targeting efficiency to the cancer cells.[4] Therefore, the development of novel nanoplatforms for circumventing these hitches for the delivery of PTX is urgently needed.[6]

In today's pharmaceutical arena, prodrug polymers have significantly been appreciated as drug carriers to improve therapeutic efficacy endowed with reduced toxicities.[7,8] Several hydrophobic drug molecules could be easily conjugated to the hydrophilic polymers to afford amphiphilic prodrugs, which are self-assembled into the core−shell nanoarchitectures.[9] Pioneering investigations utilized various polysaccharides as the hydrophilic units to accomplish prodrug polymers.[10] Pullulan (PULL) is an exopolysaccharide comprising maltotriose residues and being extensively employed to fabricate drug cargos due to its outstanding biocompatibility and modifiability.[11] The backbone of the tailor-made PULL could be facially conjugated with the hydrophobic drugs (*i.e.*, PTX) *via*

Received: October 13, 2022
Accepted: December 29, 2022
Published: January 12, 2023

https://doi.org/10.1021/acsami.2c18422
ACS Appl. Mater. Interfaces 2023, 15, 4441−4457

redox-responsive disulfide (−SS−) linkages. The resulting prodrug nanoscaffolds could elute the conjugated drug molecules into the cancer cells in response to their elevated intracellular redox potential (>20 mM of glutathione, GSH), causing improved drug delivery performances with attenuated off-targeted toxicities.[7]

Recent studies established that the active targeting by surface modification of the drug carriers with a ligand, which binds to the complementary receptors overexpressed on the cancer cells, would facilitate the intracellular drug delivery. It could amplify the therapeutic efficacy of the drugs with minimal adverse effects.[12] Transferrin (TF), an endogenous blood glycoprotein, has long been recognized as a ligand targeting the transferrin receptors (TFRs) overexpressed on the lung cancer cells.[13] Hence, TF-decorated and redox-responsive PULL/PTX prodrug NPs could be strategically developed to achieve an outstanding therapeutic benefit in the patients with metastatic lung cancer. To the best of our knowledge, no univocal study has yet been conducted to fabricate such biomaterials and explore their drug delivery potentials.[14]

In the current investigation, a redox-responsive PULL−SS−PTX conjugate was initially accomplished by grafting PTX to the chemically modified PULL backbone and its self-assembled NPs were further functionalized with TF, yielding TF−PULL−SS−PTX NPs. These redox-responsive prodrug NPs were subsequently assessed for their credibility to suppress the metastatic lung cancer through an array of *in vitro* and *in vivo* investigations relative to the corresponding redox-insensitive nanovesicles (PULL−CC−PTX NPs) and Taxol as controls.

2. MATERIALS AND METHODS

2.1. Materials. PTX (Dalian Meilun Biotech., China), PULL (M_W, ∼200 KD, Shanghai Aladdin Biochemical Technology, China), TF (M_W, 75−80 KD, Wuhan Huatesheng Biological Technology, China), chloroacetic acid (Tianjin Damao Chemical Reagent, China), ethylenediamine (ED, Shanghai Macleans Biochemical Technology, China), succinic anhydride (SA, Tianjin Damao Chemical Reagent, China), 3,3′-dithiodipropionic acid (DTPA, Shanghai TCI Chemical Industry, China), acetyl chloride (Tianjin Damao Chemical Reagent, China), 4-dimethylaminopyridine (DMAP, Shanghai Aladdin Biochemical Technology, China), 1-ethyl-3-(3-dimethylaminopropyl)-carbodiimide hydrochloride (EDC·HCl, Shanghai Aladdin Biochemical Technology, China), *N*-hydroxysuccinimide (NHS, Shanghai Aladdin Biochemical Technology, China), triethylamine (TEA, Tianjin Damao Chemical Reagent, China), dithiothreitol (DTT, Dalian Meilun Biotech, China), B16−F10 cells (murine melanoma cells, Chinese Academy of Sciences cell bank, China), LLC−luc (luciferase-expressing Lewis lung carcinoma cells, iCell Bioscience Inc., Shanghai), BEAS−2B cells (human bronchial epithelial cells, Kunming Cell Bank, China), Dulbecco's modified Eagle's medium (DMEM, high glucose, Dalian Meilun Biotech, China), coumarin 6 (Beijing Solarbio Science & Technology, China), 4′,6-diamidino-2-phenylindole (DAPI, Beijing Solarbio Science & Technology, China), 3-[4,5-dimethylthiazol-2-yl]-2,5-diphenyl-tetrazolium bromide (MTT, Dalian Meilun Biotech, China), HPR-conjugated secondary antibody (cat no: C31430100, Thermo Fisher Scientific, China), immobilon Western ECL reagent (cat no: MAO186, Dalian Meilun Biotech, China), anti-β-actin antibody (cat no: MA1-140, Thermo Fisher Scientific, USA), CD71 antibody and its isotype control (cat no: 13-6890, Thermo Fisher Scientific, USA), Alexa Fluor 488-labeled secondary antibody (cat no: A-11001, Thermo Fisher Scientific, China), 1,1-dioctadecyl-3,3,3,3-tetramethylindotricarbocyanine iodide (DiR, Dalian Meilun Biotech, China), and D-luciferin potassium (cat no: MB1834, Dalian Meilun Biotech, China) were used.

2.2. Synthesis of PULL−CC−PTX and PULL−SS−PTX. Carboxymethyl pullulan (CM−PULL) was synthesized based on a published protocol.[11] Precisely, chloroacetic acid (6 mL, 55% w/v) and NaOH (6 mL, 10% w/v) were admixed with a dispersion of PULL in isopropanol (2 g/12 mL) and the reaction mixture was continuously agitated at 70 °C for 6 h. It was then washed with excess methanol/water system (4:1 v/v) 3 times, dialysed (M_W, 10 KD) against distilled water for 2 days, and freeze-dried.

The grafting of ED on CM−PULL was accomplished adopting an earlier reported method.[15] Briefly, EDC (460 mg, 2.4 mmol), NHS (280 mg, 2.4 mmol), and TEA (222 mg, 2.2 mmol) were introduced to an aqueous dispersion of CM−PULL (700 mg/30 mL) and the reaction mixture was activated overnight with stirring. ED (1.08 g, 18.0 mmol) was then added to it, and the reaction was continued at room temperature for 24 h. The product (CM−PULL−ED) was precipitated in excess methanol, filtered, washed with a methanol/water system (4:1 v/v) 2 to 3 times, and dialysed (M_W, 10 KD) against distilled water for 2 days before being freeze-dried.

To synthesize 3,3′-dithiodipropionic anhydride (DTPA−A), DTPA (1.0 g, 4.8 mmol) was refluxed in the presence of acetyl chloride (5 mL) at 65 °C for 4 h[16]. The unreacted acetyl chloride was then removed under the reduced pressure of a rotary evaporator (RE2000-A, Shanghai Yarong Biochemistry Instrument, China). The product was precipitated in cold ether, filtered, and vacuum-dried.

PTX−SA and PTX−DTPA were afforded by reacting PTX with SA and DTPA−A, respectively, according to the previously published procedure.[17] Precisely, PTX (0.311 g, 0.36 mmol), EDC (0.211 g, 1.1 mmol), and SA (0.06 g, 0.6 mmol) or DTPA−A (0.115 g, 0.6 mmol) were dissolved in dichloromethane (DCM, 10 mL) under stirring. After 2 h, DMAP (45.0 mg, 0.37 mmol) was introduced and the reactions were continued for 48 h at room temperature. The DCM was removed under reduced pressure, and the products were precipitated with acidic solution (0.1 M HCl, 30 mL), filtered, washed with copious water, and vacuum-dried.

Following the published protocol, PTX−SA and PTX−DTPA were separately reacted with CM−PULL−ED to afford PULL−CC−PTX and PULL−SS−PTX, respectively.[18] In brief, EDC (0.0566 g, 0.3 mmol), NHS (0.0338 g, 0.3 mmol), and PTX−SA (0.137 g, 0.14 mmol) or PTX−DTPA (0.150 g, 0.14 mmol) were dissolved in dimethyl sulfoxide (DMSO, 3 mL), and TEA (32.5 μL) was added dropwise to the reaction mixture. After 24 h of activation, a solution of CM−PULL−ED in DMSO (137 mg/2 mL) was slowly introduced, and the pH of the reaction mixtures was adjusted to 8.0 with 5 mM sodium carbonate/sodium bicarbonate buffer and allowed to stir at room temperature for 24 h. The products were then dialysed (M_W, 10 KD) against water for 2 days and freeze-dried.

2.3. Characterization of PULL/PTX Conjugates. *2.3.1. ^{1}H NMR.* PTX, PULL, various freeze-dried samples including CM−PULL, CM−PULL−ED, PULL−CC−PTX and PULL−SS−PTX, and related intermediates were dissolved in DMSO-d_6 or D_2O-containing tetramethylsilane (TMS, 0.1 volume %) and analyzed by an ARX-300 spectrometer (BRUKER, Germany) to record their ^{1}H NMR spectra.

2.3.2. FT−IR. FT−IR spectroscopy (Bruker IFS55, JASCO, Germany) was utilized to scan various samples fixed in KBr pellets over a wavenumber range of 4000−1000 cm^{-1}.

2.3.3. SEM. The samples (*i.e.*, PULL, PULL−CC−PTX, and PULL−SS−PTX) were sputter-coated with gold, and their surface morphologies were observed under a scanning electron microscope (magnification, 2000 X, ZEISS Sigma 300, Sigma, China), functioning at an acceleration voltage of 3 kV.

2.4. Fabrication of PULL−CC−PTX NPs and PULL−SS−PTX NPs. Accurately weighed amounts (10 mg) of PULL−CC−PTX and PULL−SS−PTX were separately dissolved in DMSO (0.2−0.5 mL) and slowly introduced in Milli-Q water (2 mL) at variable stirring speed (400−800 rpm). The resulting mixtures were probe-sonicated (BioSafer 659−92, China) for 3 min (working time, 3 s and stopping time, 2 s) exploiting different ultrasonic powers (10−35 W). The preparations were dialysed (M_W, 10 KD) against water for 24 h to remove DMSO.[19] The samples were then suitably diluted in distilled

https://doi.org/10.1021/acsami.2c18422
ACS Appl. Mater. Interfaces 2023, 15, 4441−4457

water and transferred to polystyrene latex cells. Subsequently, their particle size, zeta potential, and PDI values were examined by a Malvern zetasizer (Malvern, UK) at 25 °C with a detector angle of 90°. The effects of three process parameters—DMSO/water ratios, stirring speed, and ultrasonic power—on their diameters were also investigated.

2.5. Surface Functionalization of PULL−SS−PTX NPs with TF and Characterization. To an aqueous dispersion of the optimal PULL−SS−PTX NPs (10 mg/2.5 mL), EDC (14 mg, 0.07 mmol), NHS (8 mg, 0.07 mmol), and TEA (0.6 μL) were introduced. After 1 h of activation, TF (0.5 mg) was added and the reaction mixture was gently stirred at room temperature for 12 h. The TF-conjugated scaffold was then dialysed (M_W, 100 KD) against water for 24 h.[20] TF conjugation at the surfaces of PULL−SS−PTX NPs was quantified using a BCA assay kit (Beyotime Institute of Biotechnology, Suzhou, China) and the experiment was performed according to the manufacturer's instructions.[21,22] Moreover, the freeze-dried scaffold was characterized by ^{1}H NMR and FT−IR analyses according to the methods described in Section 2.3. The zeta potential, size, and polydispersity index (PDI) values of TF−PULL−SS−PTX NPs were also examined by a Malvern zetasizer (Malvern, UK) and compared with those of PULL−CC−PTX NPs and PULL−SS−PTX NPs.

2.6. TGA, DSC, and P-XRD Analyses. *2.6.1. TGA.* PTX, PULL, and different freeze-dried samples (*viz.*, PULL−CC−PTX NPs, PULL−SS−PTX NPs, and TF−PULL−SS−PTX NPs) were examined on a thermal analyzer (TGA 550, METTLER TOLEDO, Switzerland) at a heating rate of 10 °C min^{-1} under continuous nitrogen purging (50 mL min^{-1}) within a wide temperature range (25−600 °C).

2.6.2. DSC. Various specimens were placed on a sealed aluminum pan, and their thermal curves were recorded on a differential scanning calorimeter (DSC Q200, METTLER TOLEDO, Switzerland) over a wide temperature range of 0−300 °C (heating rate, 10 °C min^{-1}) under continuous nitrogen flow (50 mL min^{-1}).

2.6.3. P-XRD. The samples were examined between 3° and 60° (2θ) on a powder X-ray diffractometer (Dandong Haoyuan Instrument, China) operating at an anode voltage of 40 kV and input current of 40 mA.

2.7. Redox Sensitivity and Drug Release Patterns. PULL−CC−PTX NPs, PULL−SS−PTX NPs, and TF−PULL−SS−PTX NPs (0.2 mg/mL) were incubated with DTT (0 and 10 mM) at 37 °C for 4 h under gentle agitation. These samples were subsequently scanned under a UV−Vis spectrophotometer (NanoDrop One, Thermo Scientific, China) at wavelengths ranging between 190 and 420 nm (wavelength interval, 1 nm). The zeta potential, average hydrodynamic size, and PDI values of these dispersions were also measured by a Malvern zetasizer (Malvern, UK). Moreover, various specimens were embedded on carbon-coated TEM grids (Beijing Zhongjingkeyi Technology, China) and viewed under a transmission electron microscope (TEM, Hitachi, HT7700, Japan), which was operated at an acceleration voltage of 80 kV.

Various NPs were introduced to 20 mL of release medium (PBS, pH 7.4/ethanol, 7:3 v/v) under gentle agitation (100 rpm) in the absence or presence of DTT (0 and 10 mM, respectively) at 37 °C.[23] The aliquots were withdrawn at different time intervals and the released drug concentration was examined by the HPLC method.[4]

2.8. Storage and Colloidal Stabilities. Different NPs diluted in deionized water (1 mg/mL) were stored at 4 °C for 7 days and analyzed by a Zetasizer (Nano ZS, Malvern, UK) to determine their diameter and PDI values.[24] To monitor their colloidal stability, NPs were also incubated in PBS (pH 7.4) supplemented with 10% FBS at 37 °C under constant agitation (100 rpm) and the changes in their size and PDI values were recorded up to 72 h.[25]

2.9. Cell Culture Experiments. *2.9.1. Cellular Uptake.* Coumarin 6-loaded scaffolds were formulated by dissolving coumarin 6 (0.12 mg/mL) and PULL/PTX conjugate (20 mg/mL) in DMSO and followed analogous protocols of NP formation. Their cellular uptake efficiencies on B16−F10 cells were then assessed based on a previously published method.[26] Briefly, cells were seeded on a glass bottom dish at a density of 2 × 10^5 cells/well and following 24 h of incubation, these were treated with coumarin 6-loaded NPs in serum-free medium for 1, 2, and 4 h at 37 °C. The cells were then washed with cold PBS three times and fixed with 4% (w/v) paraformaldehyde for 30 min before counterstaining the cell nuclei with DAPI for 10 min. The cells were subsequently visualized under a confocal laser scanning microscope (CLSM, Nikon C2 Plus, Japan).

The treated cells were harvested, washed, and suspended in PBS, and the intracellular fluorescence intensity of coumarin 6 was quantitatively analyzed exploiting a flow cytometer (BD FACS Calibur, USA) at an acquisition of 10,000 events per histogram.[27]

2.9.2. Cytotoxicity. The cytotoxic potentials of PULL−CC−PTX NPs, PULL−SS−PTX NPs, TF−PULL−SS−PTX NPs, and Taxol against B16−F10, LLC−luc, and BEAS−2B cells were examined following the MTT assay protocol.[23] Precisely, the cells were subcultured into 96-well plates (2 × 10^3 cells/well) and incubated in a humidified chamber (37 °C, 5% CO_2) (Thermo, USA) for 24 h. The cells were then treated with varying doses of samples and incubated for 48 h. Subsequently, the multiwell pates were incubated with the MTT reagent for 4 h and their absorbance was recorded on a microplate reader (BMG Labtech, FLUOstar Omega, Germany) at 570 nm after solubilizing the formazan crystals in DMSO.

2.9.3. TFR Targetability. 2.9.3.1. TFR Expression Study. Western blot and flow cytometry protocols were adopted to assess TFR expression levels (CD71, TFR1) on BEAS−2B, B16−F10, and LLC−luc.[28] Briefly, the cells were harvested and lysed by freshly prepared RIPA lysis buffer supplemented with a protease inhibitor (1:100 dilution). The protein contents of the cell lysates were determined by the BSA assay protocol following collection by centrifugation (12,000 rpm, 15 min) at 4 °C. The samples with equal protein content (20 μg) were diluted with 5× loading buffer, boiled for 10 min, and subjected to SDS-polyacrylamide gel (10%) electrophoresis at a constant voltage (80 V). These were then transferred to a PVDF membrane at 150 mA for 100 min and blocked with Tris-buffered saline containing 5% (w/v) skim milk for 2 h at room temperature. The membrane was subsequently incubated with an anti-CD71 antibody (1:500 dilution) overnight at 4 °C and treated with a HPR-conjugated secondary antibody (1:10000 dilution) for 1 h following washing with TPST buffer. The blots were finally detected using the Immobilon Western ECL reagent. The membrane was also probed with an anti-β-actin antibody (1:2000 dilution) for standardization of the samples.

The cells (5 × 10^5) were incubated with a CD71 antibody and its corresponding isotype control overnight at 4 °C. These were then washed 3 times, collected by centrifugation (400 g for 5 min), and resuspend in 3% BSA/PBS containing a fluorochrome-labeled secondary antibody. Following incubation for 30 min at room temperature, the cells were analyzed by flow cytometry at an excitation wavelength of 488 nm and emission wavelength of 585 nm.

2.9.3.2. TFR-Mediated Cellular Trafficking. TFR-overexpressed LLC−luc cells (2 × 10^5 cells/well) were cultured and treated with coumarin 6-loaded PULL−SS−PTX NPs and TF−PULL−SS−PTX NPs in an analogous protocol as described previously.[26] Following staining with DAPI, the cells were visualized under CLSM.[26] The fluorescence intensity of the treated cells was also determined using a flow cytometer.[27]

The competitive effect of cellular uptake was also examined by pre-incubating the cells with excess free TF (25 μM) for 2 h before treating with coumarin 6-loaded TF−PULL−SS−PTX NPs.[29] The treated cells were then viewed under CLSM and analyzed by a flow cytometer.

2.10. Animal Experiments. Male C57BL/6 mice and Sprague−Dawley rats were supplied by the Laboratory Animal Center (Shenyang Pharmaceutical University, China), and the experimental protocols were approved by the Animal Ethical Committee, Shenyang Pharmaceutical University, China (SCXK-Liao-2020-0001).

2.10.1. Anticancer Activities on B16−F10 Melanoma Mouse Model. B16−F10 cells (4 × 10^5 cells/animal) were intravenously injected *via* tail veins of the mice (20−22 g) to develop a melanoma lung metastasis model.[4] The tumor-bearing mice were randomized into 5 different groups and intravenously treated with PBS (negative

https://doi.org/10.1021/acsami.2c18422
ACS Appl. Mater. Interfaces 2023, 15, 4441−4457

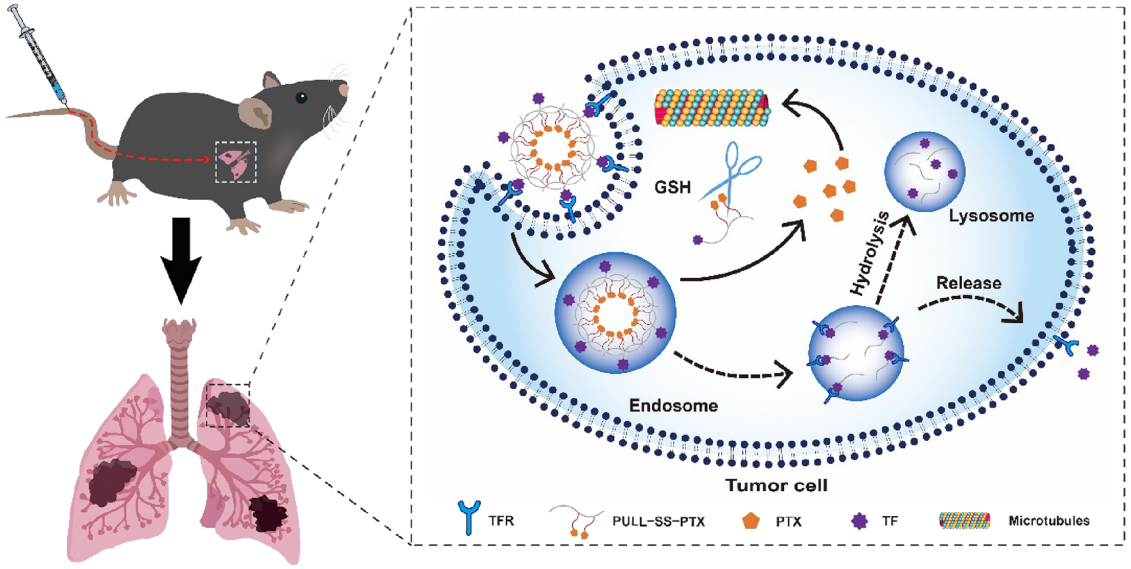

Figure 1. Schematic representation of the intravenous delivery of TF-decorated prodrug NPs (TF−PULL−SS−PTX NPs) and their GSH-triggered drug release behavior with the fate of TF residues in the metastatic lung cancer cells.

control), PULL−CC−PTX NPs, PULL−SS−PTX NPs, TF−PULL−SS−PTX NPs, and Taxol (positive control) containing an equivalent PTX dose (10 mg/kg) on the 4th, 6th, 8th, 10th, 12th, and 14th day after the tumor cell implantation. On the 16th day, the lungs were harvested from the sacrificed mice of various groups to capture their images. Following fixation with 4% paraformaldehyde solution, the lung weights were recorded and the lung tissues stained with hematoxylin and eosin (H&E) were observed under a microscope (NIKON Eclipse ci, Japan).[30]

2.10.2. Targetability and Anticancer Activities on the LLC−Luc Melanoma Mouse Model. The lung metastasis model was also established by intravenous injection of LLC−luc cells (3×10^6 cells/animal) to the mice (20−22 g).[31] After 15 days, the mice were intravenously treated with DiR-labeled PULL−SS−PTX NPs and TF−PULL−SS−PTX NPs. Animals were sacrificed 24 h after treatment and the fluorescence signals in their lungs and other major organs were examined under an IVIS imaging system (Lumina XRMS Series III, PerkinElmer, USA).[32]

Tumor-bearing mice were divided into 4 treatment groups after 8 days of LLC−luc cell inoculation and intravenously administered PBS (negative control), PULL−SS−PTX NPs, TF−PULL−SS−PTX NPs, and Taxol (positive control). Various preparations containing an equivalent PTX dose of 10 mg/kg were used to treat the animals at every alternative day 6 times. On the 20th day, D-luciferin (150 mg/kg) was given to the mice by intraperitoneal injection and *in vivo* and *ex vivo* bioluminescence signals of the lungs representing the tumor burden of animals were captured using an IVIS imaging system.[33] The lung tissues were also visualized under a microscope after H&E[4] and Ki-67 staining.[34]

2.11. Toxicity Studies. *2.11.1. In Vivo Systemic Toxicity.* To assess the systemic toxicity, the change in body weight of different groups of mice was recorded during the treatment period. The blood samples were collected *via* the retro-orbital sinus of the mice on the 20th day. Following centrifugal separation at 3000*g* for 10 min, the serum was analyzed for various hepatic and renal function tests. The vital organs of the sacrificed animals were also harvested, and fixed with 4% paraformaldehyde solution, and the tissue specimens were stained with H&E to observe under a microscope.[4]

2.11.2. Ex Vivo Hemolysis Study. The hemolytic assay was conducted according to the reported protocol.[9] Precisely, Sprague−Dawley male rat blood (6 mL) was collected and normal saline (60 mL) was mixed with it by inversion. Subsequently, the mixture was centrifuged at 1500 rpm for 15 min and the supernatant was discarded. The centrifuging and washing steps were repeated 3−4 times. A required volume of saline was then added to yield the concentration of red blood cell (RBC) suspension of 2%. The concentrations of various samples including PULL−SS−PTX NPs, TF−PULL−SS−PTX NPs, and Taxol were then adjusted to 80 to 4 $mg{\cdot}mL^{-1}$ PTX with the normal saline and 2% RBC suspension. These samples were incubated in a water bath at 37 °C for 2 h and centrifuged at 1500 rpm for 5 min. The absorbance of the collected supernatants was measured on a UV−Vis spectrophotometer (AOE Instruments, UV1000, China) at 540 nm. In this experiment, the mixture of normal saline and 2% RBC suspension and mixture of Milli-Q water and 2% RBC suspension were considered as the negative control and positive control, respectively. The studies were performed in triplicate. The hemolysis (%) was estimated based on the following expression:

$$\text{hemolysis (\%)} = \frac{A_s - A_0}{A_{100} - A_0} \times 100\%$$

A_0, A_{100}, and A_s symbolize the absorbances of the negative control, positive control, and tested samples, respectively.

2.12. Statistical Analysis. The numerical data of various experiments were represented as mean ± SD. The results of different groups were compared exploiting Student's *t* test (two-tailed) and one-way analysis of variance (ANOVA). The *p* values below 0.05 were considered as statistically significant.

3. RESULTS AND DISCUSSION

3.1. Synthesis and Characterization of PULL−CC−PTX and PULL−SS−PTX. In the current investigation, the redox-responsive PULL/PTX-based prodrug NPs decorated with a tumor homing ligand, TF, were presented for efficient chemotherapeutic agent delivery against metastatic lung cancer. Following their intravenous administration, TF−PULL−SS−PTX NPs could rapidly be accumulated in the lungs and exhibit triggered drug release in response to the amplified levels of GSH in the cancer cells, causing an enhanced therapeutic outcome (Figure 1).[4] On the other hand, the TF-PULL conjugates might be partly recirculated back to the surfaces of the cell membrane and TF could be released. The residual conjugates could be degraded in the cells by the lysosomes.[35,36] The precursor conjugate of such nanoscaffolds (*viz.*, PULL−SS−PTX) and a redox-insensitive control template (*i.e.*, PULL−CC−PTX) were synthesized

https://doi.org/10.1021/acsami.2c18422
ACS Appl. Mater. Interfaces 2023, 15, 4441−4457

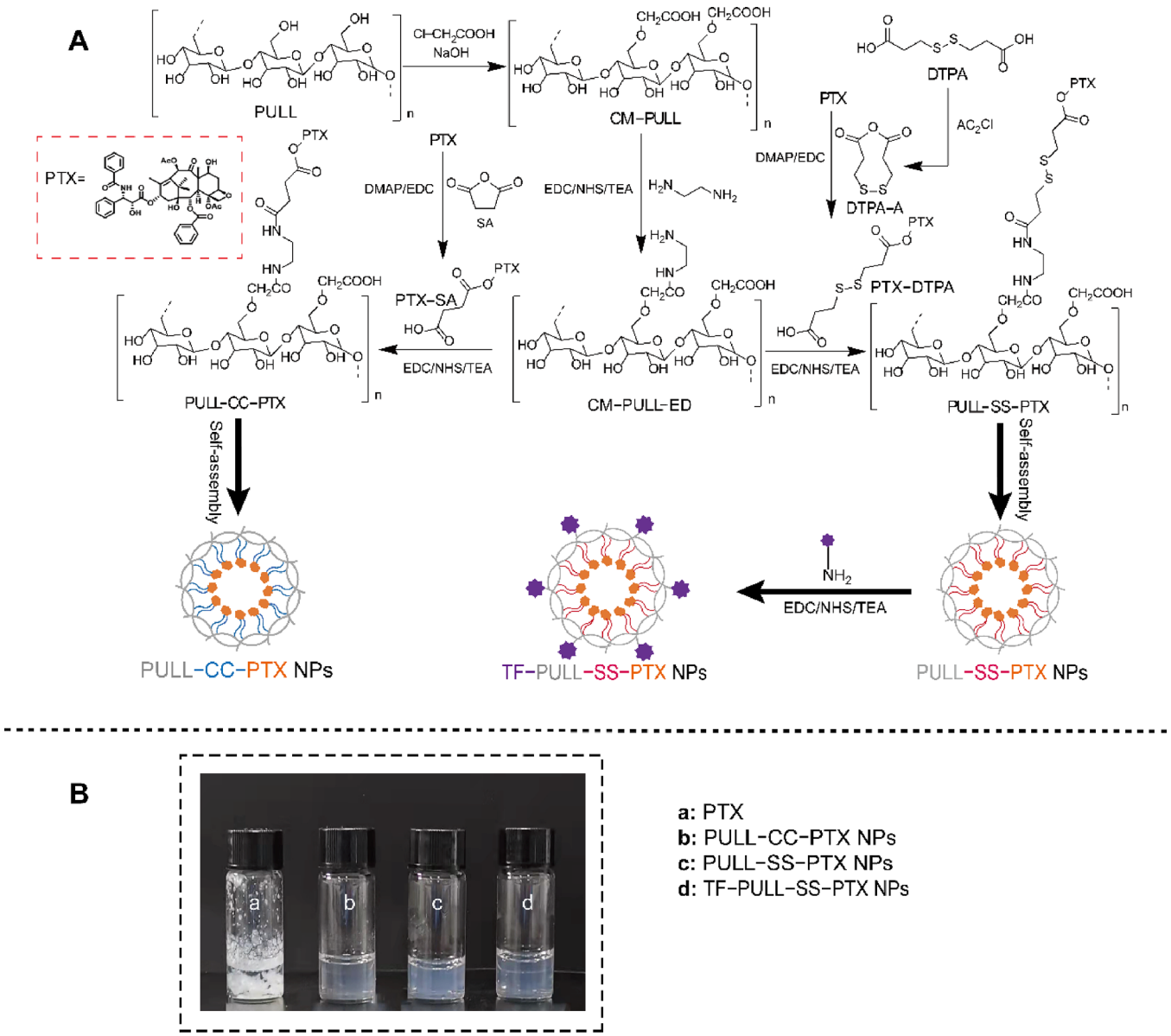

Figure 2. Synthetic schemes of redox-sensitive and redox-insensitive PULL/PTX conjugates and corresponding NPs (A). Photographs of the physical appearances of aqueous dispersions of native PTX and different NPs (B).

according to the scheme illustrated in Figure 2A. CM−PULL was initially afforded employing the Williamson ether synthesis protocol.[11] The hydroxyl groups of PULL chains were alkalized in the presence of sodium hydroxide to produce PULL alkoxide, which was subsequently reacted with monochloroacetic acid to obtain CM−PULL *via* an S_N^2-type reaction mechanism. Exploiting EDC/NHS coupling chemistry, ED was further grafted to the CM−PULL backbone to introduce amino groups[15] followed by covalently attaching with PTX−SA and PTX−DTPA to produce PULL−CC−PTX and PULL−SS−PTX, respectively.[18] PTX was esterified with SA and DTPA−A to synthesize PTX−SA and PTX−DTPA, respectively.[17] To completely avoid unwanted dimeric product (*viz.*, PTX−SS−PTX), DTPA was dehydrated by refluxing with acetyl chloride to get cyclic anhydride DTDP−A before esterification reaction.[16]

The ^{1}H NMR spectra of pristine PULL and its conjugates are compared in Figure 3A. The native PULL displayed anomeric and hydroxyl protons resonating at δ 5.3−4.8 ppm and sugar ring protons between δ 3.9 and 3.3 ppm[11]. In the NMR spectra of CM−PULL and CM−PULL−ED, the signals of methylene protons (−CH_2−) appeared at δ 4.2 ppm and between δ 3.3 and 3.2 ppm, respectively.[15] The degree of substitution (DS) of CM−PULL was calculated by a back-titration protocol, and it was found to be 0.23.[11] The DS value for CM−PULL−ED calculated from the integration ratios of methylene protons (−CH_2−) to anomeric protons was 0.08 The carboxylic acid (−COOH) signal of DTPA at δ 12.4 ppm disappeared in the ^{1}H NMR spectrum of DTPA−A, conferring its successful synthesis.[16] In the ^{1}H NMR spectra of PTX−SA and PTX−DTPA, the characteristic signal of 2′-CH of pure PTX was shifted from δ 4.6 ppm to δ 5.6 ppm. Moreover, the emergence of the methylene (−CH_2−) proton peak (δ 3.0−2.6 ppm) and carboxyl proton peak (δ 12.4 ppm) validated the structures of PTX−SA and PTX−DTPA.[17] Successful synthesis of PULL−CC−PTX and PULL−SS−PTX was supported by the presence of ^{1}H NMR signals of aromatic protons of PTX (δ 8.0−7.0 ppm) and sugar ring protons of

https://doi.org/10.1021/acsami.2c18422
ACS Appl. Mater. Interfaces 2023, 15, 4441−4457

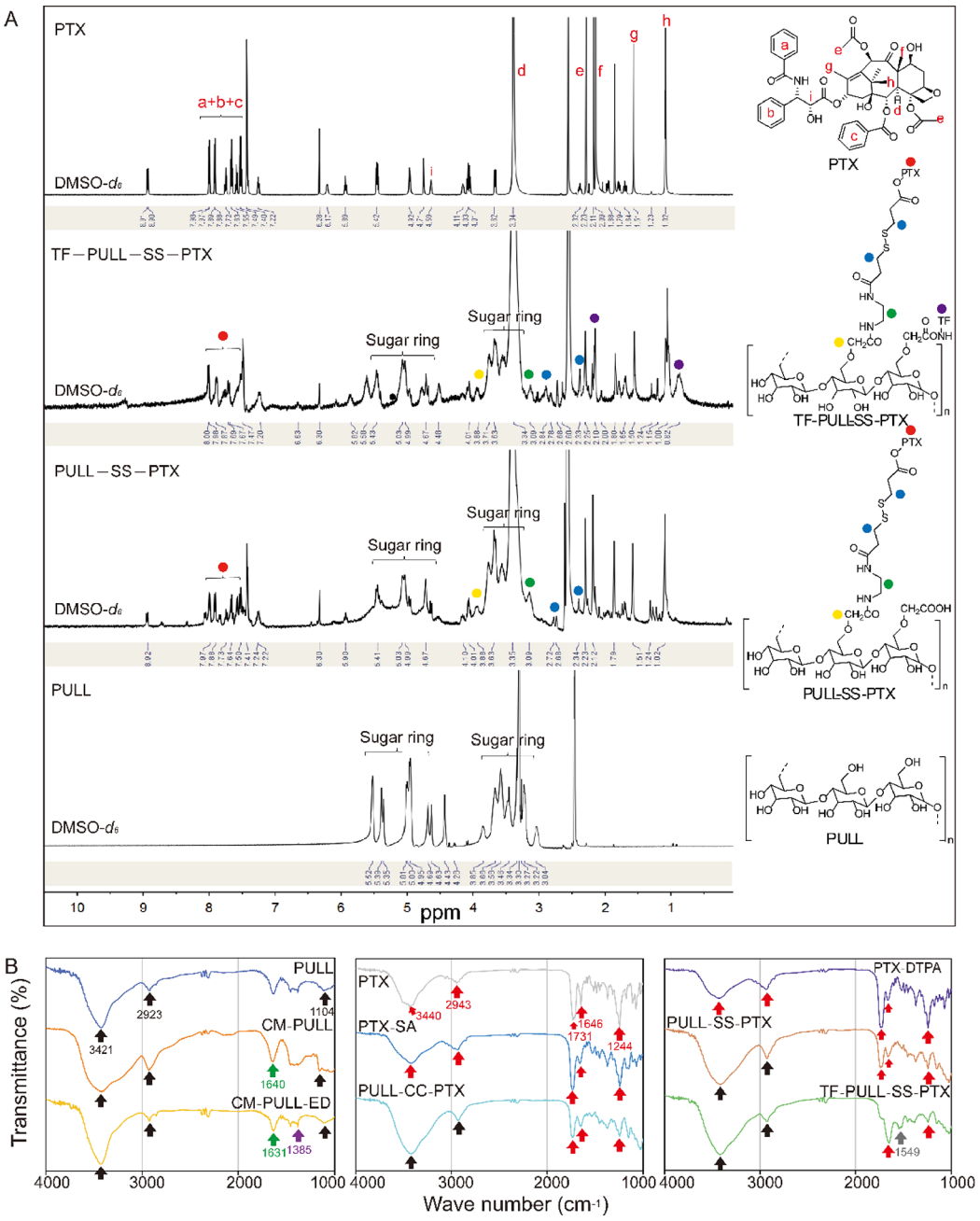

Figure 3. ^{1}HMR (A) and FT−IR (B) spectra of native PULL, PTX, and their conjugates and various intermediates.

Table 1. Drug Loading and Zeta potential, Size, and PDI of Various Nanoscaffolds after DTT (0 and 10 mM) Treatment[a]

		zeta potential (mV)		diameter (nm)		PDI	
scaffolds	drug loading (%)	DTT (0 mM)	DTT (10 mM)	DTT (0 mM)	DTT (10 mM)	DTT (0 mM)	DTT (10 mM)
PULL−CC−PTX NPs	42.2 ± 1.5	−11.4 ± 0.6	−11.2 ± 0.7	117.7 ± 3.2	118.5 ± 1.1	0.183 ± 0.024	0.184 ± 0.024
PULL−SS−PTX NPs	37.2 ± 1.0	−12.6 ± 2.3	−17.9 ± 0.9	133.5 ± 2.0	252.4 ± 5.9	0.149 ± 0.035	0.374 ± 0.014
TF−PULL−SS−PTX NPs	37.5 ± 1.2	−13.3 ± 0.8	−20.7 ± 1.9	162.6 ± 7.4	257.6 ± 5.4	0.106 ± 0.052	0.360 ± 0.032

[a]Data presented as mean ± SD, n = 3.

PULL (δ 5.0−3.5 ppm). The PTX loading contents on PULL−CC−PTX and PULL−SS−PTX were 42.2% and 37.2%, respectively (Table 1), which were calculated from the integration area ratios of the peak at δ 1.6 ppm, assigned to methyl groups of PTX, to a peak of PULL at δ 5.0 ppm. The drug loading was also estimated by measuring PTX concentration in PULL−SS−PTX through the HPLC method following its incubation with 20 mM DTT for 4 days. The results were well-collaborated with the outcome of ^{1}H NMR analyses.

Figure 3B illustrates the FT−IR spectra of native PULL and its conjugates. In the IR spectrum of unmodified PULL, various distinct absorption signals such as OH stretching, CH_2 stretching, and glycosidic (α-(1,4) and α-(1,6)) stretching

https://doi.org/10.1021/acsami.2c18422
ACS Appl. Mater. Interfaces 2023, 15, 4441−4457

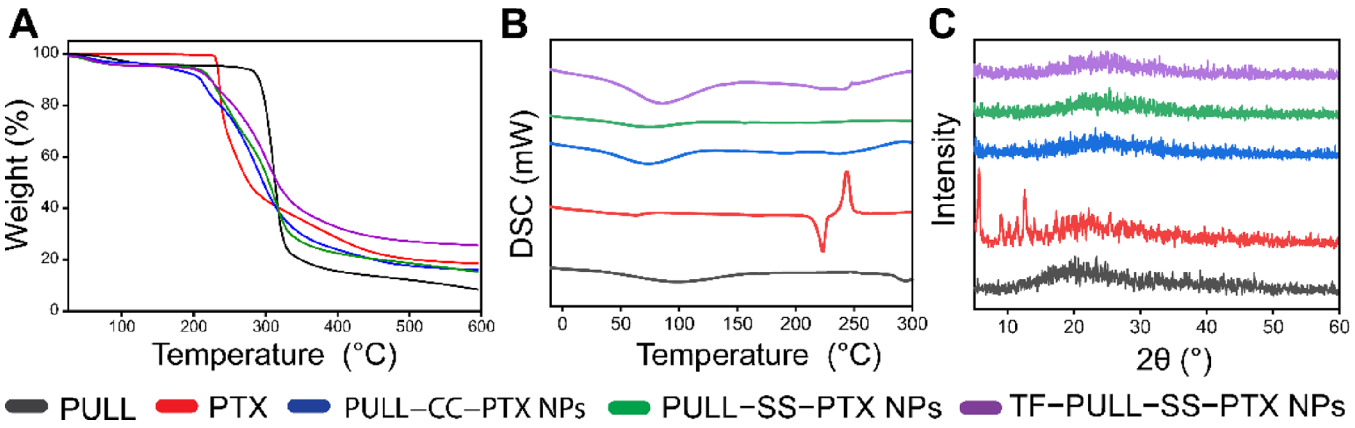

Figure 4. TGA patterns (A), DSC thermograms (B), and XRD patterns (C) of native PULL, pure PTX, and various freeze-dried PULL/PTX NPs.

were evident at 3420, 2923, and 1104 cm^{-1}, respectively.[11] CM−PULL possessed a new peak at 1640 cm^{-1}, which was ascribed to the symmetrical stretching vibration of the carboxylate (COO^-) group. In the FT−IR spectrum of CM−PULL−ED, the characteristic peak of −C═O was blue-shifted to 1631 cm^{-1} and the C−N stretching signal appeared at 1385 cm^{-1}.[15] The FT−IR spectrum of pristine PTX presented its distinctive absorption bands of OH, CH, C═O ester, C═O amide, and C−O− stretching at 3440, 2943, 1732, 1646, and 1244 cm^{-1}, respectively. Most of these PTX peaks remained unaltered in the FT−IR spectra of PTX−SA and PTX−DTPA. The conjugation of the diacid linker to PTX molecules intensified the C−H stretching signal and shifted the O−H stretching band to lower frequencies.[4] The FT−IR spectra of PULL−CC−PTX and PULL−SS−PTX exhibited typical absorption peaks from PTX (~1655 cm^{-1}) and PULL (~3420 cm^{-1}), indicating that PTX was successfully conjugated to the PULL backbone.

The morphological appearances of native PULL and freeze-dried conjugates were also examined. The SEM photograph of the pristine PULL showed its distinctive polyhedral structure with fibrous surfaces (Figure S1).[11] The grafting of hydrophobic PTX molecules onto the PULL chains affected their folding and nucleation behavior, eventually altering the morphological appearances of the conjugates. The SEM images of PULL−CC−PTX portrayed interconnected honeycomb structures, while PULL−SS−PTX exhibited networks with agglomerated globules. A reduced intermolecular hydrogen bonding density within these conjugates could reduce their stiffness, which caused fusion of the particles during the lyophilization process.[37]

3.2. Fabrication of PULL−CC−PTX NPs and PULL−SS−PTX NPs. The obtained conjugates were subsequently self-assembled through a nanoprecipitation method. The intrinsic amphiphilicity of the prodrug polymers could favor their self-assembly into NPs in the aqueous environment, with hydrophobic PTX as the cores and hydrophilic PULL chains as the shells (Figure 2A,B).[9] The effects of three process parameters—the ratios between DMSO and water, stirring speed, and ultrasonic power—on their sizes were investigated. The sizes of the NPs were decreased with increasing ratios between DMSO:H_2O, stirring speed, and ultrasonic power (Table S1). A diminution in the conjugate concentration owing to an increase in DMSO (solvent) volume could decrease the viscosity of the organic phase. This could exhibit a lower mass transfer resistance and increase the diffusion efficiency of the conjugate−solvent phase into water (non-solvent), forming smaller particles.[38] Additionally, an intense agitation could prevent the agglomeration of immature NPs more successfully and produced particles with a smaller size.[39] On the other hand, at a higher power of ultrasound, the intensity of particle−cavitation interactions could increase and result in a reduced particle size of the NPs.[40] Based on these observations, the ratio between DMSO:H_2O of 0.5:2, stirring rate of 800 rpm, and ultrasonic power of 195 W were considered as optimal process parameters, yielding smaller size particles of PULL−CC−PTX NPs and PULL−SS−PTX NPs (118 and 134 nm, respectively) with a unimodal size distribution (PDI values, 0.183 and 0.149, respectively) (Figure S2, Table S1, and Table 1). Their zeta potential values were about −12 mV, indicating the existence of anionic CM−PULL residues on the outer layers of the NPs. The aqueous dispersion of pristine PTX displayed obvious white precipitates, while both PULL−CC−PTX NPs and PULL−SS−PTX NPs showed slightly bluish opalescence due to their characteristic Tyndall effects (Figure 2B), further suggesting the formation of amphiphilic nanoaggregates in the solution.[4] The lower critical micelle concentration (CMC) value of PULL−SS−PTX (0.036 mg/mL) also indicated the stabilities of the scaffolds in aqueous media (Figure S3).[41]

3.3. Surface Functionalization of PULL−SS−PTX NPs with TF. The carboxylic functional groups of the PULL-SS-PTX NPs were used for NHS/EDC activation followed by conjugation with TF (Figure 2A).[20] TF conjugation onto NPs was quantitated by the BCA assay, and the conjugation efficiency was found to be 55.8% (0.0279 mg TF/mg of NPs). The particle size of TF−PULL−SS−PTX NPs was around 163 nm, and thus, the TF conjugation could enhance the particle size of the parent NPs (Table 1). The functionalization of NPs with negatively charged TF slightly deceased their surface charges. This was consistent with the previous reports.[21] The results also demonstrated that the particle size distribution and physical appearance did not obviously alter after TF conjugation (Table 1, Figure S2, and Figure 2B).

The surface functionalization of NPs was validated by ^1H NMR and FT-IR spectral analyses (Figure 3A,B). In the NMR spectrum of TF−PULL−SS−PTX NPs, the appearance of new peaks at δ 2.1 and 0.8 ppm confirmed the presence of TF amide (−CONH) and methyl ($-CH_3$) groups, respectively, conferring the attachment of TF onto the surfaces of PULL−SS−PTX NPs. The drug loading content value of TF−PULL−SS−PTX NPs calculated based on integration ratios of PTX

https://doi.org/10.1021/acsami.2c18422
ACS Appl. Mater. Interfaces 2023, 15, 4441−4457

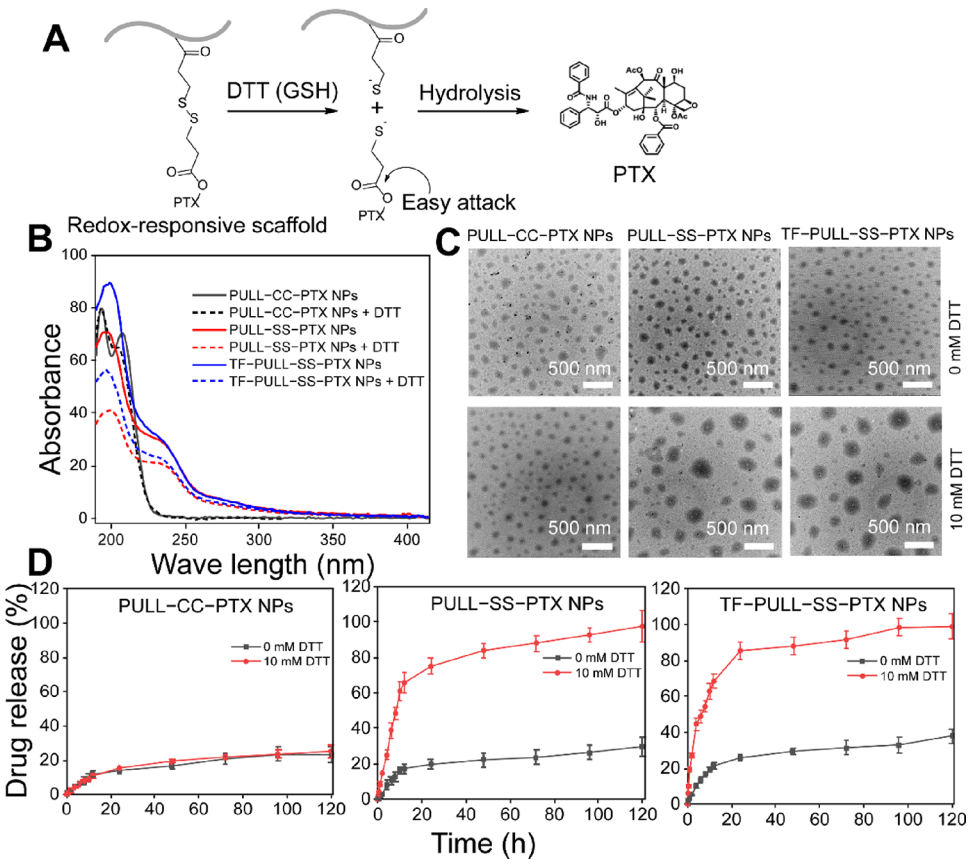

Figure 5. Cleavage of disulfide bonds of redox-sensitive PULL/PTX NPs in the presence of DTT, a simulatant of GSH (A). Effects of redox stress on different prodrug NPs assessed by UV−Vis spectroscopy (B) and TEM studies (C) following DTT (0 and 10 mM) treatment for 4 h. PTX release patterns of various scaffolds under simulated normal and redox environments (0 and 10 mM DTT, respectively) (D) (data represented as mean ± SD, n = 3).

and PULL remained close to that of PULL−SS−PTX NPs (Table 1). In the FT−IR spectrum of TF-functionalized NPs, the bands matched to C═O stretching vibrations (1650 cm^{-1}) and N−H bending vibrations (1549 cm^{-1}) represented the peptide bonds of the TF backbone. These peaks were more intensive and pronounced relative to the nonfunctionalized NPs, providing strong evidence for NP functionalization.[42]

3.4. Thermal Properties and P-XRD Patterns. The thermal behavior and P-XRD patterns of pristine PULL, PTX, and different prodrug NPs were compared (Figure 4A−C). The TGA pattern of native PULL demonstrated three stages of thermal degradation.[11] An initial stage of mass loss (∼7%) within 30−280 °C was caused by the structural water evaporation. The second phase of thermal decomposition of polysaccharide macromolecular chains was observed within 290−340 °C (weight loss, ∼80%). Lastly, the thermal degradation of PULL sugar rings was evidenced above 340 °C (Figure 4A). On the other hand, PTX was thermally stable up to 240 °C and approximately 70% of PTX was degraded at 395 °C.[5] The synthesized prodrug NPs displayed variable thermal decomposition profiles as compared to native PULL and PTX. A faster weight loss of prodrug NPs within 200−300 °C relative to pristine PULL could be ascribed to the thermal degradation of the substituted sites and decomposition of the polysaccharide backbone.[11] Interestingly, TF-functionalized NPs displayed a higher thermal stability with a greater percent of char residues at 600 °C as compared to the non-functionalized prodrug NPs. A higher energy was possibly required to break the bonds of the surface-attached TF of the NPs, which eventually increased the thermal stability of TF−PULL−SS−PTX NPs.[43]

The DSC thermogram of native PULL illustrated a broad endothermic signal at around 50−150 °C attributed to the physisorbed water evaporation (Figure 4B).[11] Pure PTX depicted a sharp endothermic peak corresponding to its melting point at 223 °C followed by a degradation exotherm at 244.3 °C, accredited to its decomposition point.[5] The characteristic thermal events of PTX including its melting and decomposition peaks were almost disappeared in various prodrug NPs. It indicated that drug molecules were in an amorphous state or disordered-crystalline phase in these scaffolds.[4] As compared to PULL−CC−PTX NPs and PULL−SS−PTX NPs, the water desorption signal of TF−PULL−SS−PTX NPs became more obvious. This was probably due to the absorbed water molecules of TF residues stabilized through intermolecular H-bonding interactions.[44]

Pristine PULL depicted no sharp P-XRD peaks, indicating its amorphous nature. However, it revealed a relatively intense and broad signal at a 2θ value of 20°, which was ascribed to the hydrogen bond-assisted structural rearrangement of the polysaccharide chains (Figure 4C).[11] PTX displayed several well-resolved and sharp diffraction signals at 2θ of 5.8°, 9.0°, 11.3°, and 12.6°, which confirmed its crystalline characteristics.[4] The specific P-XRD peak of native PULL became comparatively broader in the case of prodrug NPs, implying that the intramolecular hydrogen bonding networks of PULL

https://doi.org/10.1021/acsami.2c18422
ACS Appl. Mater. Interfaces 2023, 15, 4441−4457

Table 2. Results of the *In Vitro* Drug Release Profiles of Prodrug NPs under Simulated Physiological (0 mM DTT) and Redox (10 mM DTT) Conditions

				correlation coefficient, r^2							diffusion coefficient (cm^2/min)	
scaffolds	DTT conc.	DE (%)	MDT (h)	zero order	first order	Higuchi	Hixson Crowell	Korsemeyer–Peppas	release exponent, (n)	gel characteristic constant, k_{KP}	initial, D_I	late, D_{LWR}
PULL–CC–PTX NPs	0 mM	17.99	27.78	0.831	0.855	0.964	0.543	0.949	0.67	0.014	0.37×10^{-15}	0.53×10^{-15}
	10 mM	18.93	29.98	0.839	0.864	0.971	0.557	0.958	0.68	0.014	0.41×10^{-15}	0.58×10^{-15}
PULL–SS–PTX NPs	0 mM	22.32	30.23	0.724	0.764	0.898	0.454	0.903	0.66	0.021	1.81×10^{-15}	0.78×10^{-15}
	10 mM	81.04	20.45	0.661	0.940	0.860	0.424	0.907	0.60	0.092	18.18×10^{-15}	8.46×10^{-15}
TF-PULL–SS–PTX NPs	0 mM	28.87	29.17	0.740	0.789	0.914	0.457	0.942	0.52	0.041	3.16×10^{-15}	1.61×10^{-15}
	10 mM	86.43	15.27	0.622	0.952	0.837	0.363	0.906	0.43	0.180	37.55×10^{-15}	16.38×10^{-15}

chains were disrupted after conjugation of PTX residues.[11] The distinctive crystalline signals of PTX were also vanished upon its grafting to the PULL backbone, suggesting that PTX was molecularly dispersed in the NPs. This result showed a good agreement with the DSC outcomes.

3.5. Redox Sensitivity. Dithiothreitol (DTT, 10 mM) was used as a prevailing simulant of GSH to mimic the reductive microenvironment of the cancer cells. It is less vulnerable to the oxidative degradation relative to GSH and could facilitate the cleavage of the disulfide (−SS−) bonds of nanoscaffolds (Figure 5A).[23] To investigate their redox sensitivity, prodrug NPs were exposed to 10 mM DTT for 4 h and examined by UV−Vis spectroscopy, DLS, and TEM studies. As illustrated in Figure 5B, the UV−Vis absorption spectrum of PULL−CC−PTX NPs remained unaltered following DTT treatment, indicating their redox-insensitive properties. On the contrary, PULL−SS−PTX NPs and TF−PULL−SS−PTX NPs exhibited characteristic absorption bands around 200 nm under a simulated nonreductive state, corresponding to the PTX residues. Following exposure to DTT, the absorption maxima of their absorption peaks were drastically declined. This was attributed to the disulfide bond cleavage in the presence of reductive sulfhydryl groups of DTT, leading to partial detachment of PTX molecules from these scaffolds.[45] The hydrodynamic diameters of PULL−SS−PTX NPs and TF−PULL−SS−PTX NPs were significantly increased after 4 h of incubation with DTT ($p < 0.05$), while no notable change in the particle size was evidenced for the control scaffolds (*i.e.,* PULL−CC−PTX NPs) (Table 1). DTT-triggered cleavage of disulfide linkages of redox-sensitive NPs resulted in the destabilization of their hydrophobic cores with enlarged particle sizes.[10] The zeta potential values of PULL−SS−PTX NPs and TF−PULL−SS−PTX NPs under reducing conditions were significantly decreased as compared to the non-reducing state ($p < 0.05$) (Table 1). This ensured the presence of anionic sulfhydryl (−SH) moieties on the outer surfaces of the NPs after DTT treatment.[45] On the other hand, the zeta potential values of PULL−CC−PTX NPs were almost unaltered under non-reductive and reductive conditions (Table 1). The PDI value of PULL−CC−PTX NPs was also stable even after DTT treatment (Table 1), indicating homogeneous particle population under both normal and simulated reductive conditions. However, the PDI values of PULL−SS−PTX NPs and TF−PULL−SS−PTX NPs under simulated reductive conditions were significantly altered relative to that of under non-reductive states ($p < 0.05$). The results of DLS studies were well collaborated with the TEM outcomes. Various scaffolds were observed as uniformly scattered spherical particles under TEM with dark inner regions and gray periphery, which might correspond to PTX-enriched and PULL-enriched domains, respectively.[4] When exposed to 10 mM DTT, PULL−CC−PTX NPs depicted no substantial structural transformation and almost retained their original appearances. This signified their stability in the simulated reductive environment. In contrast, PULL−SS−PTX NPs and TF−PULL−SS−PTX NPs revealed structural transition from more compact to dissociated irregular-shape and larger-size architectures (Figure 5C). Thus, the redox sensitivity of PULL−SS−PTX NPs and TF−PULL−SS−PTX NPs could be efficiently exploited for the targeted drug delivery to the lung cancer cells with enhanced therapeutic efficacy.[11,46]

3.6. Redox-Triggered Drug Release. The drug release behaviors of PULL−SS−PTX NPs and TF−PULL−SS−PTX NPs were investigated under simulated redox environments of cancer cells and compared to the corresponding insensitive scaffolds (*i.e.,* PULL−CC−PTX NPs) (Figure 5D).[10] Both sensitive and insensitive NPs exhibited significantly reduced PTX release rates in the absence of DTT (∼14−26% drug release within 24 h). Interestingly, as compared to PULL−CC−PTX NPs, the sensitive scaffolds displayed extremely augmented drug elution rates in the presence of 10 mM DTT ($p < 0.05$), which could be accredited to their greater redox sensitivity. Upon exposure to DTT media, the disulfide pendants (−SS−) of the prodrug NPs were degraded, yielding a hydrophilic thiol intermediate (PTX−SH). This could easily hydrolyze the ester bonds located at the β-position (Figure 5A),[4] resulting in an accelerated PTX release profile (∼75−86% drug release within 24 h) with greater mean dissolution time (MDT) and dissolution efficiency (DE) values (Table 2). The prodrug NPs endowed with distinct redox-triggered drug release properties might be promising for the targeted drug delivery to the lung tumor microenvironments bearing amplified levels of GSH[45].

PTX elution profiles of insensitive and sensitive NPs under a simulated reduction state were best fitted to the Higuchi and first-order models, respectively, with correlation coefficient values close to unity (Table 2).[11] The calculated n values signified that the PTX release from NPs was mostly driven by anomalous diffusion under both conditions.[2] Exceptionally, a Fickian diffusion phenomenon was dominated for the drug release patterns of TF−PULL−SS−PTX NPs under the reduction state. Thus, PTX molecules were typically released *via* both polymer chain relaxation and diffusion processes.[11] Different k_{KP} values under simulated physiological and reduction states also conferred that the geometric and structural characteristics of the prodrug NPs were altered with the modification of drug release conditions (Table 2).[2]

https://doi.org/10.1021/acsami.2c18422
ACS Appl. Mater. Interfaces 2023, 15, 4441−4457

The late diffusion coefficients (D_L) of sensitive scaffolds were obviously lower as compared to that of initial diffusion coefficient (D_I) values. This was ascribed to their initial burst release profiles (up to 24 h) followed by a slower drug elution over 48−120 h.

3.7. Stability of Prodrug NPs. Various traditional drug-loaded NPs are often unstable, hindering their usefulness in clinical applications.[23] To access the storage stability of prodrug NPs, their size changes as a function of time were monitored after incubation at 4 °C. These NPs displayed excellent storage stability without obvious variation in their average diameter and size distribution over 1 week at 4 °C (Figure S4A,B). The hydrophilic PULL sheath around the hydrophobic PTX cores and high negative surface charges could impart electrostatic repulsive forces among NPs, leading to an improved stability of these systems.[4] Subsequently, their colloidal stability was also investigated. These NPs maintained a monodisperse distribution with no significant change in their particle size and PDI values within 72 h in PBS (pH 7.4) supplemented with 10% v/v FBS (Figure S4C,D). Thus, the prodrug NPs presented an outstanding colloidal stability under simulated physiological conditions. Notably, the nanoscaffolds with good colloidal stability could be suitable in achieving a prolonged *in vivo* circulation time and augmented tumor accumulation.[23]

3.8. Cellular Uptake. The cellular uptake capacity of coumarin 6-labeled PULL/PTX prodrug NPs was investigated exploiting CLSM on B16−F10 cells. DAPI, a blue-fluorescent DNA stain, was employed to visualize the cell nucleus.[4] The green fluorescent dots of coumarin 6 were detected within the cell cytoplasm following treatment with various NPs, and the fluorescence intensity was augmented with increasing incubation time from 1 to 4 h (Figure S5A). This indicated that NPs were efficiently internalized into the lung cancer cells and their cellular uptake processes were time-dependent.[23] These negatively charged NPs could electrostatically interact with the cationic segments of the cell membrane and eventually internalize into the cells. An entropy gain-driven depletion could also cause their adsorption onto the cell membrane. The redox-insensitive smaller size scaffolds (PULL−CC−PTX NPs) exhibited a noticeably greater intracellular fluorescence signal than redox-sensitive NPs. Upon exposure to intracellular elevated level of GSH, different redox-responsive NPs could quickly disassemble and the eluted coumarin 6 undergo protonation under an acidic micro-environment of the cancer cells, obviously reducing its fluorescence intensity. On the contrary, the insensitive NPs showed a higher stability in the cellular environment and coumarin 6 remained loaded into these nanovesicles, causing a substantially increased fluorescence signal.[4] The cellular uptake efficiency of redox-sensitive and insensitive NPs on B16−F10 cells was also quantified by flow cytometric analyses, and the results were in good agreement with the outcomes of CLSM (Figure S5B,C).[23]

3.9. Cytotoxicity. The cytotoxic potentials of different prodrug NPs and Taxol were investigated on two lung cancer cells (*i.e.*, mouse melanoma B16−F10 and LLC−luc cells) and human non-tumorigenic bronchial epithelial BEAS−2B cells by the MTT assay protocol following 48 h of treatment.[23] Various scaffolds effectively suppressed the cell growth in a dose-dependent manner, and their half maximal inhibitory concentration (IC_{50}) values are summarized in Table 3 and Figure S6.

Table 3. IC_{50} Values of Various Prodrug NPs and Taxol in Different Cell Lines Following 48 h of Treatment[a]

	IC_{50} values (μg/mL)		
scaffolds	B16−F10	LLC−luc	BEAS−2B
PULL−CC−PTX NPs	10.1 ± 0.6	25.7 ± 2.2	10.1 ± 1.8
PULL−SS−PTX NPs	9.6 ± 5.0	13.9 ± 3.6	41.7 ± 4.4
TF−PULL−SS−PTX NPs	7.2 ± 0.7	12.3 ± 4.0	41.2 ± 5.4
Taxol	0.1 ± 0.1	0.4 ± 0.1	0.4 ± 0.1

[a]Data presented as mean ± SD, n = 3.

Taxol and prodrug NPs demonstrated varying levels of sensitivity toward two cancer cell lines (*i.e.*, B16F10 and LLC−luc), depicting variable antiproliferative potentials (Figure 6A). Different prodrug NPs portrayed a reduced cytotoxicity on the cancer cells as compared to Taxol, accredited to their delayed release profiles of the conjugated PTX.[4] GSH-triggered rapid PTX release rate of redox-sensitive NPs in the cancer cells led to a greater growth suppressive activity than that of insensitive control NPs. Interestingly, redox-responsive NPs illustrated a lower cytotoxicity than Taxol on noncancerous BEAS-2B cells (Figure 6A), indicating their superior cancer cell selectivity. An attenuated drug release rate of redox-responsive prodrug NPs in the normal lung epithelial cells bearing a lower level of GSH caused such reduced cytotoxicity.[23] This could potentially suppress their drug-related adverse effects on the healthy cells relative to Taxol.[4]

3.10. TFR Targetability. Previous studies reported that TFR expression is more abundant in malignant cells than in healthy cells.[47] TFR, an iron import machinery, could overexpress in the cancer cells and contribute in intracellular iron accumulation, inducing cell proliferation. This also makes TFR as an attractive target for cancer therapeutics.[48] Non-tumorigenic epithelial BEAS−2B cells and various lung cancer cell lines (*viz.*, B16−F10, LLC−luc) were screened for TFR protein expression by western blotting (Figure 6B,C).[28] The healthy BEAS−2B cells and cancerous B16−F10 cells showed a very limited expression of receptors. Interestingly, TFR expression in LLC−luc cells was significantly higher than B16−F10 cells ($p < 0.05$). Flow cytometry analyses also revealed that the membrane expression of TFR on whole intact LLC−luc cells was substantially greater than that of BEAS−2B and B16−F10 cells ($p < 0.05$) (Figure 6D).[20]

Taking advantage of overexpressed TFR, we attempted to evaluate the cellular trafficking efficiency of PULL−SS−PTX NPs and TF−PULL−SS−PTX NPs on LLC−luc cells by CLSM analyses (Figure 6E).[4] TF-modified NPs loaded with coumarin 6 illustrated significantly enhanced intracellular accumulation as compared to PULL−SS−PTX NPs, suggesting the importance of TF modification. When the cells were preincubated with free TF, the cellular uptake of TF−PULL−SS−PTX NPs was dramatically reduced (Figure 6E). Free TF could block the TFR receptors and competitively inhibit the uptake of TF−PULL−SS−PTX NPs by declining receptor availability. This evidenced that the cellular internalization of TF−PULL−SS−PTX NPs could take place *via* TFR receptor-mediated trafficking together with non-specific adsorption-mediated endocytosis.[29] The CLSM results of TFR targetability of TF−PULL−SS−PTX NPs on LLC−luc cells were further validated by flow cytometry analyses (Figure 6F,G).[4] The cellular uptake abilities of TF−PULL−SS−PTX NPs on TFR monoclonal antibody-treated LLC−luc cells were also dramatically reduced as compared to that on the untreated

https://doi.org/10.1021/acsami.2c18422
ACS Appl. Mater. Interfaces 2023, 15, 4441−4457

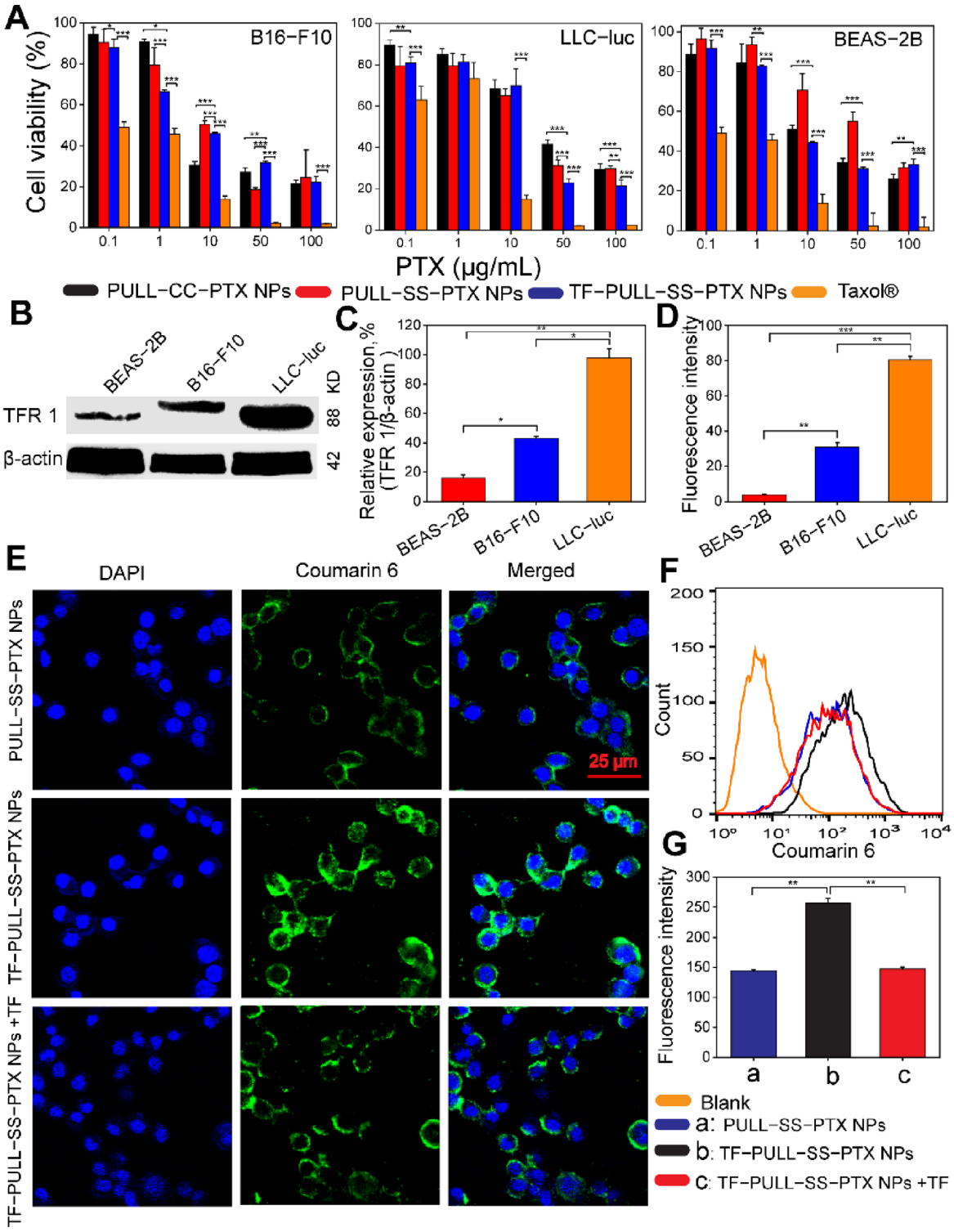

Figure 6. Cytotoxic potentials of various prodrug NPs and Taxol on B16−F10, LLC−luc, and BEAS−2B cells after 48 h of incubation (A) (n = 5). Representative western blots (B), corresponding densitometry graphs (C), and results of flow cytometry analyses (D) of the TFR expression in BEAS−2B, B16−F10, and LLC−luc cells (n = 3). Cellular internalization of coumarin-6-loaded redox-sensitive NPs on LLC−luc cells analyzed by confocal laser scanning microscopy (E) and flow cytometry (F) and their quantitative signal intensity (G) (n = 3) (data represented as mean ± SD, *p < 0.05, **p < 0.01, and ***p < 0.001).

cells, which further confirmed the TFR targetability of the scaffolds (Figure S7). The cellular uptake capacities of TF−PULL−SS−PTX NPs with different levels of TF conjugations were enhanced with increasing their TF contents (Figure S8). As a consequence of a greater cellular internalization, TFR-targeted NPs could show significantly higher *in vivo* antitumor efficacies as compared to the nontargeted counterparts. Moreover, the cellular uptake efficiency of TF−PULL−SS−PTX NPs on BEAS-2B cells (low TFR expression) was significantly reduced than that on LLC-luc cells (high TFR

https://doi.org/10.1021/acsami.2c18422
ACS Appl. Mater. Interfaces 2023, 15, 4441−4457

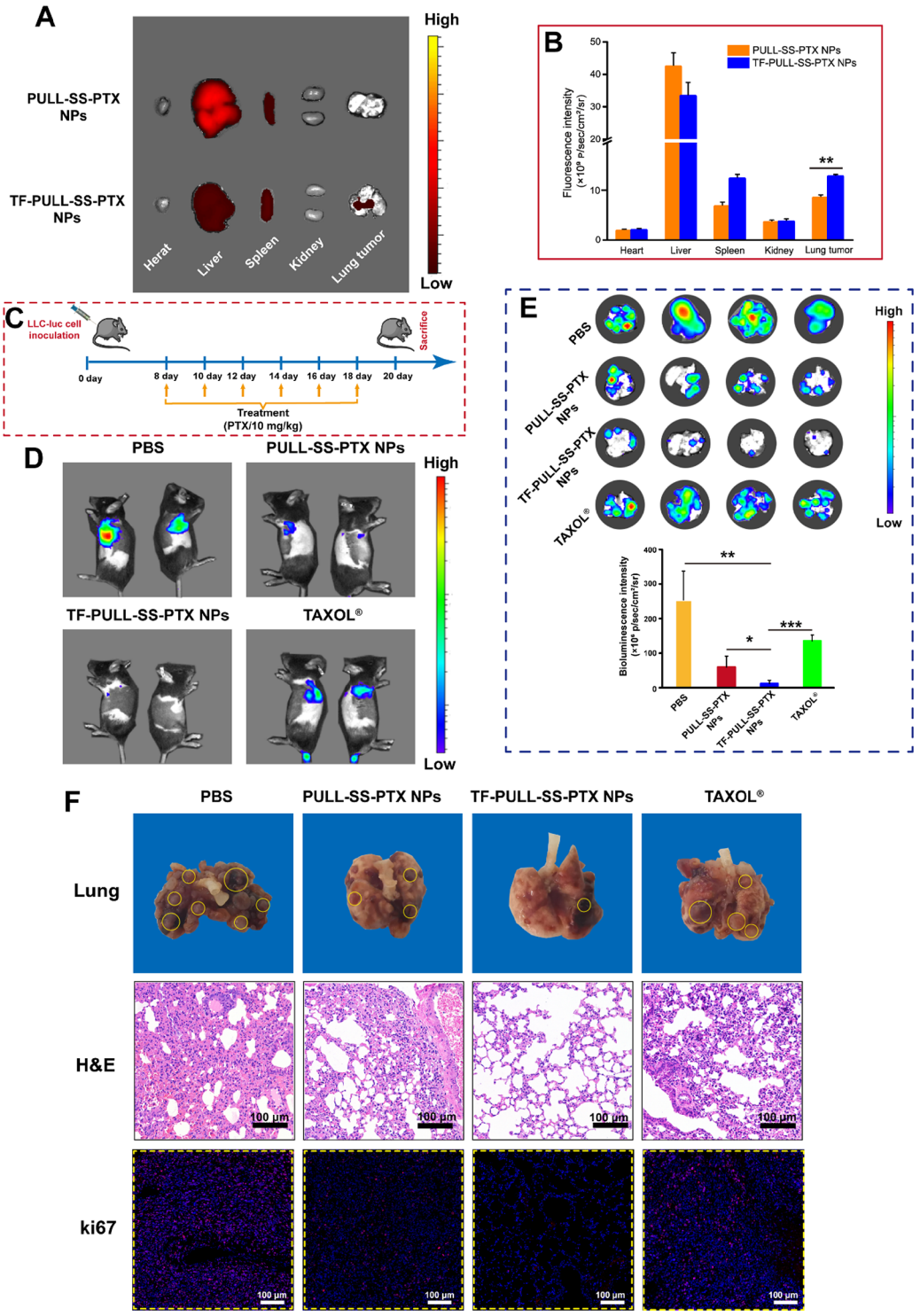

Figure 7. Fluorescence images of various organs of C57BL/6 mice captured 24 h after administration of DiR-labeled NPs (A) and their quantitative analyses (B) (n = 3). Schematic representation of the *in vivo* experimental protocol of antitumor efficacy testing of prodrug NPs on the LLC−luc metastatic lung cancer mice model (C). Representative bioluminescence images of the dorsal planes of the treated animals (D) and bioluminescence signals of the harvested lungs and their quantitative analyses (E) (n = 4) after treatment with different scaffolds. Representative photographs of the excised lungs collected at the 20th day and the images of lung tissues after H&E and Ki67 staining (F) (n = 3) (data represented as mean ± SD, *p < 0.05, **p < 0.01, and ***p < 0.001).

expression) (p < 0.05) (Figure S9), implying the safety profiles of the TF-modified scaffolds.

3.11. Biodistribution, *In Vivo* Anticancer Activities, and Effects of TFR Targetability. Following the promising *in vitro* findings, tumor-targeting capability and biodistribution of PULL−SS−PTX NPs and TF−PULL−SS−PTX NPs were investigated. Initially, the TFR-overexpressing lung cancer model was established through intravenous inoculation of LLC cells constitutively expressing luciferase to C57BL/6 mice. The progression of tumor growth in living animals was monitored

https://doi.org/10.1021/acsami.2c18422
ACS Appl. Mater. Interfaces 2023, 15, 4441−4457

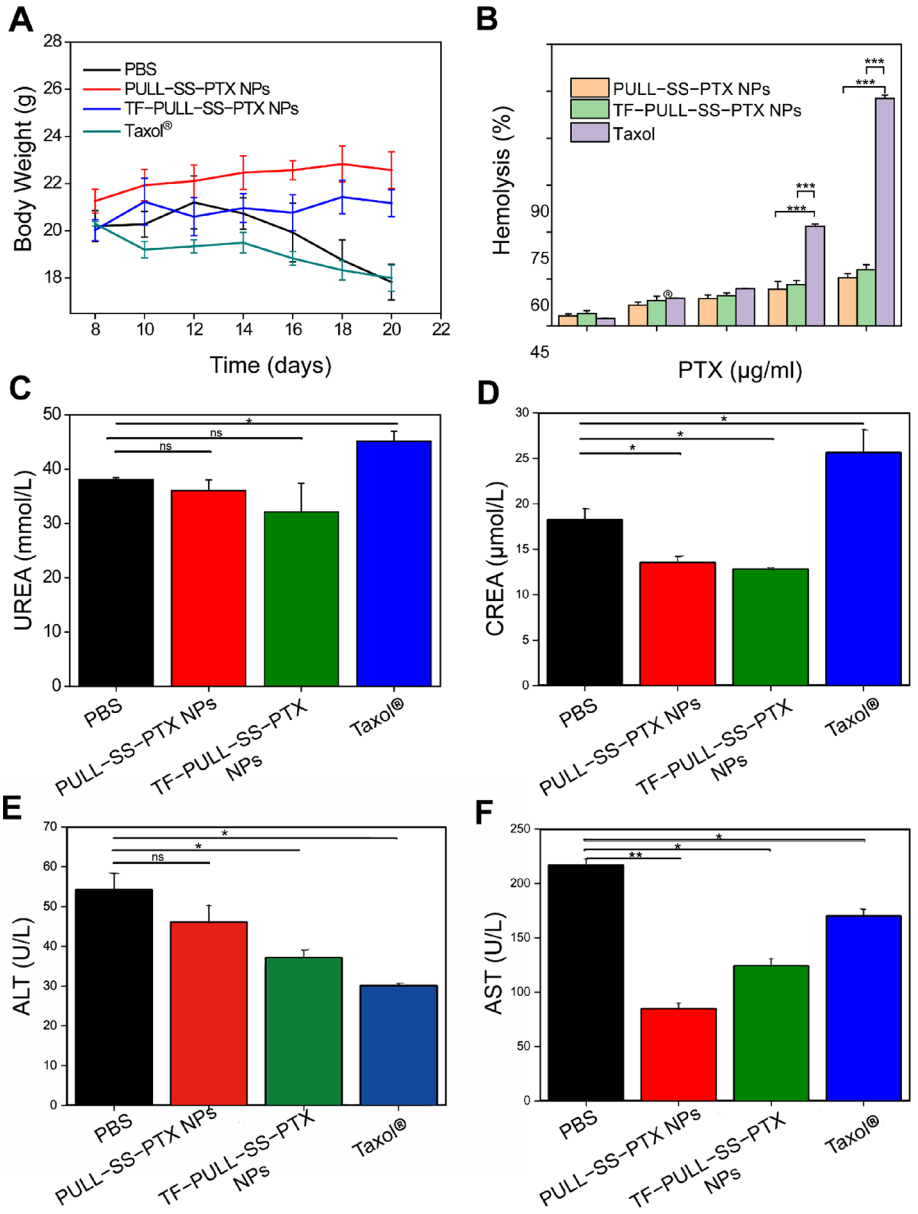

Figure 8. Body weight changes of animals of different treatment groups during *in vivo* antitumor efficacy testing experiments (A) (n = 4) and hemolysis of PTX−SS−PTX NPs, TF−PULL−SS−PTX NPs, and Taxol (equivalent PTX, 4−80 μg/mL) (B) (n = 3). Plasma concentrations of UREA (C) and CREA (D) for kidney toxicity and ALT (E) and AST (F) for liver toxicity tests following treatment with different scaffolds (n = 4) (data represented as mean ± SD, *p < 0.05, **p < 0.01, and ***p < 0.001).

by examining the bioluminescence of implanted cancer cells, and obvious lung metastases were observed on the 7th day after cell inoculation.[31] On the 15th day, DiR-labeled NPs were intravenously administered to mice bearing metastatic orthotopic LLC−luc tumors and *ex vivo* fluorescence signals of various harvested organs were captured after 24 h. PULL−SS−PTX NPs were primarily distributed in the liver and spleen, without accumulation in lungs (Figure 7A,B). Liver and spleen uptake could be ascribed to the mononuclear phagocyte system-mediated clearance of systemically delivered foreign particles.[49] The liver accumulation of the NPs could also be due to their liver-targeting PULL backbone.[50] Interestingly, a strong fluorescence signal was detected in the lungs of mice treated with TF−PULL−SS−PTX NPs. An obviously superior localization of TF−PULL−SS−PTX NPs on orthotopically established tumor tissues relative to PULL−SS−PTX NPs (p < 0.05) could be attributed to their ability to target TFRs.[51]

The greatly enhanced tumor accumulation provided us a strong rationale to investigate *in vivo* antitumor activity of TFR-targeted NPs as compared to PULL−SS−PTX NPs and Taxol in the metastatic orthotopic LLC−luc lung cancer model following their intravenous administration.[31] A total of six doses (equivalent PTX, 10 mg/kg body weight) administered at every alternative day were received by various groups of animals (Figure 7C). The insensitive scaffold (PULL−CC−PTX NPs) was excluded from the experimental design of the LLC−luc lung cancer mice model as these NPs displayed extremely limited chemotherapeutic efficacy on the B16−F10 metastatic lung cancer mice model (Figure S10A−D).[4] Moreover, the merits of TFR targetability of TF−PULL−SS−PTX NPs on their improved *in vivo* anticancer potentials

https://doi.org/10.1021/acsami.2c18422
ACS Appl. Mater. Interfaces 2023, 15, 4441−4457

as compared to PULL−SS−PTX NPs and Taxol were not established on the B16−F10 lung cancer model (Figure S10A−D). This could be accredited to a lower expression of TFR on B16−F10 cells (Figure 6B−D). The tumor growth suppressing effects of various sensitive scaffolds and Taxol were thus investigated on the TFR-overexpressing LLC−luc lung cancer mice model exploiting bioluminescence imaging.[33]

Figure 7D illustrates the representative images of dorsal planes of the treated animals at the 20th day. Vehicle-treated mice conferred a rapid tumor progression as quantified by luciferase expression. The cells of Taxol and PULL−SS−PTX NP-treated groups proliferated sluggishly than those of the control treated group. TF−PULL−SS−PTX NPs could inhibit the tumor growth more efficiently as compared to the mice treated with the vehicle, Taxol, and PULL−SS−PTX NPs. The strongest antitumor effect of TF−PULL−SS−PTX NPs was due to the synergistic effects of their TFR-mediated cellular uptake and the redox-activated PTX release behavior.[29] On the 20th day, the mice were euthanized to harvest their lungs for further analyses. The lungs of the TF−PULL−SS−PTX NP-treated group depicted the weakest bioluminescence signals among other treatment groups, validating their superior antineoplastic efficacy (Figure 7E).[32] The excised lungs of animals were also photographed. It was observed that the tumor nodules in the lungs of TF−PULL−SS−PTX NP-treated group were drastically decreased relative to other groups (Figure 7F).

Analyses of H&E staining of the lung tissues of the vehicle-treated group demonstrated extensive metastasis distributed throughout the lung lobe. On the contrary, the lung specimen of the TF−PULL−SS−PTX NP-treated group exhibited luminal alveolar cells with a reduced number of metastatic cancer and inflammatory cells (Figure 7F).[4] Furthermore, immunofluorescence analyses of the lung sections bestowed significant suppression of cell proliferative marker Ki-67 expression with decreased violet fluorescence intensity in the experimental group treated with TF−PULL−SS−PTX NPs as compared to other treated groups ($p < 0.05$) (Figure 7F and Figure S11).[52] This conferred a distinct superiority of TF-decorated NPs in killing tumor cells after treatment.

3.12. Systemic Toxicity. The progressive body weight changes of animals over the study period were recorded to access the systemic toxicity.[4] As portrayed in Figure 8A, vehicle and Taxol intravenous injection treated groups demonstrated obvious body weight loss during the treatment period. Severe tumor development in the vehicle-treated group and high excipient-associated toxicity of Taxol caused such weight loss in animals. In contrast, the body weights of prodrug NPs treated mice were steady over the study period. In addition, PULL−SS−PTX NPs and TF−PULL−SS−PTX NPs exhibited minimal hemolysis, while Taxol drastically damaged the red cell membranes at equivalent PTX concentrations ranging from 4 to 80 μg/mL ($p < 0.05$) (Figure 8B). Thus, the prodrug strategy could considerably diminish the lethal systemic toxicity of PTX.[9] Furthermore, the histological examinations of the tissues of various vital organs of intravenously delivered prodrug NP-treated groups evidenced no cell necrosis, degeneration, inflammatory response, and other pathological changes. On the contrary, the Taxol intravenous injection-treated group showed distinct necrosis and inflammation in cardiac and splenic tissues and tubule degeneration (Figure S12). Serum UREA and CREA levels for kidney toxicity and ALT and AST levels for liver toxicity were also examined to further validate the improved safety profiles of redox-responsive prodrug NPs as compared to Taxol (Figure 8C−F). The levels of UREA, CREA, and AST of the Taxol-treated group were significantly higher than those of the prodrug NP-treated group ($p < 0.05$), implying a greater systemic safety profile and better tolerability of the nano-scaffolds. Endogenous GSH-triggered selective bioactivation of prodrug NPs in the tumor cells could obviously suppress the serious PTX toxicity to the normal cells.[4] These findings were well aligned with their *in vitro* cytotoxic effects.

4. CONCLUSIONS

In the current study, bio-reducible PULL/PTX based prodrug NPs and the corresponding TF-decorated nanoscaffolds were successfully fabricated and structurally characterized. The NPs demonstrated suitable drug loading capacity (~37%), acceptable particle sizes (134−163 nm) with a regular spherical shape, and excellent colloidal stability. When exposed to simulated reducing conditions, these NPs bearing disulfide (−SS−) pendants portrayed a sharp redox sensitivity, resulting in an accelerated cargo release (~75−86% within 24 h) relative to the control scaffold (PULL−CC−PTX NPs, ~16% within 24 h). The redox-triggered rapid release profiles caused their discriminating cytotoxicity between the cancer (IC_{50}, >14 μg/mL) and normal cells (IC_{50}, ~41 μg/mL) and an enhanced *in vivo* pharmacologic response with reduced systemic toxicities. The TF-decorated NPs were efficiently accumulated into TFR overexpressed tumor cells and consequently demonstrated an improved cancer-suppressing potential compared to the TF-free nanoscaffolds. Thus, the findings of the investigation collectively proved its hypothetical statements true. Overall, the design of TF-anchored prodrug NPs validated the efficient intracellular delivery of chemotherapeutic agents and these novel nanoscaffolds could represent an evolving treatment strategy for lung cancer therapy.

AUTHOR CONTRIBUTION

X.Z.: methodology, validation, data curation, investigation; H.G.: methodology, validation, data curation, investigation. H.B.: conceptualization, methodology, data curation, writing − original draft, supervision; H.J.: methodology, investigation; Y.C.: methodology, investigation; G.X.: methodology, investigation; X.T.: methodology, investigation; D.C.: supervision, project administration; M.Y.: conceptualization, supervision, project administration, writing − review & editing.

ASSOCIATED CONTENT

Supporting Information

The Supporting Information is available free of charge at https://pubs.acs.org/doi/10.1021/acsami.2c18422.

NMR spectra of PULL, CM−PULL, CM−PULL−ED, DTPA, DTPA−A, PTX, PTX−SA, PTX−DTPA, PULL−CC−PTX, and PULL−SS−PTX; SEM images of PULL, PULL−CC−PTX, and PULL−SS−PTX; effects of DMSO/H_2O ratios, speeding rate, and ultrasonic power on the sizes of NPs; size distribution of various prodrug NPs, formulated in optimal conditions; critical micelle concentration (CMC) value of PULL−SS−PTX; changes in size and PDI values of prodrug NPs over time after incubating them in distilled water at 4 °C; change in particle size and PDI values of these scaffolds within 72 h in PBS (pH 7.4)

https://doi.org/10.1021/acsami.2c18422
ACS Appl. Mater. Interfaces 2023, 15, 4441−4457

supplemented with 10% FBS; cellular internalization of coumarin 6-loaded prodrug NPs on B16−F10 cells; bar chart of IC_{50} values of various prodrug NPs and Taxol in different cell lines following 48 h of treatment; comparative cellular uptake behavior of the TF−PULL−SS−PTX NPs on LLC−luc cells treated with and without the TFR monoclonal antibody; cellular uptake capacities of TF−PULL−SS−PTX NPs with different levels of TF conjugations on LLC−luc cells; cellular uptake behavior of TF−PULL−SS−PTX NPs on BEAS−2B cells (low TFR expression) and LLC−luc cells (high TFR expression); *in vivo* antitumor efficacy testing on the B16−F10 metastatic lung cancer mice model; quantitative analysis of Ki-67-positive cells in lung tissues following treatment in the Lewis lung carcinoma (LLC−luc) cell bearing mice model; histological analysis (H&E staining) of the major organs following treatment with different formulations in the Lewis lung carcinoma cell-bearing mice model; HPLC method (PDF)

AUTHOR INFORMATION

Corresponding Authors

Hriday Bera − *Wuya College of Innovation, Shenyang Pharmaceutical University, 110016 Shenyang, China; Dr. B. C. Roy College of Pharmacy and Allied Health Sciences, Durgapur, India 713206*; Phone: +91-8900580914; Email: hriday.bera1@gmail.com

Dongmei Cun − *Wuya College of Innovation, Shenyang Pharmaceutical University, 110016 Shenyang, China*; Phone: +8618640041566; Email: cundongmei@163.com

Mingshi Yang − *Wuya College of Innovation, Shenyang Pharmaceutical University, 110016 Shenyang, China; Department of Pharmacy, Faculty of Health and Medical Sciences, University of Copenhagen, DK-2100 Copenhagen, Denmark*; orcid.org/0000-0003-3201-4696; Phone: +45-35336141; Email: mingshi.yang@sund.ku.dk

Authors

Xing Zhao − *Wuya College of Innovation, Shenyang Pharmaceutical University, 110016 Shenyang, China*

Haifei Guo − *Wuya College of Innovation, Shenyang Pharmaceutical University, 110016 Shenyang, China*

Huiyang Jiang − *Wuya College of Innovation, Shenyang Pharmaceutical University, 110016 Shenyang, China*

Yang Chen − *Wuya College of Innovation, Shenyang Pharmaceutical University, 110016 Shenyang, China*

Xiong Guo − *Wuya College of Innovation, Shenyang Pharmaceutical University, 110016 Shenyang, China*

Xidong Tian − *Wuya College of Innovation, Shenyang Pharmaceutical University, 110016 Shenyang, China*

Complete contact information is available at: https://pubs.acs.org/10.1021/acsami.2c18422

Author Contributions

#X.Z. and H.G. contributed equally.

Notes

The authors declare no competing financial interest.

ACKNOWLEDGMENTS

This research work was financially supported by the National Natural Science Foundation of China (grant nos. 81850410554 and 82050410448), fellowship of China Postdoctoral Science Foundation (grant no. 2021MD703857), Liaoning Pan Deng Xue Zhe Scholar (grant no. XLYC2002061), the National Natural Science Foundation of China (grant no. 82173768), and the Overseas Expertise Introduction Project for Discipline Innovation ("111Project") (grant no. D20029). D.C. thanks the Guiding Project for Science and Technology of Liaoning Province (grant no. 2019-ZD-0448) and the Ministry of Education Chunhui Program (2020) for their financial supports.

REFERENCES

(1) Sung, H.; Ferlay, J.; Siegel, R. L.; Laversanne, M.; Soerjomataram, I.; Jemal, A.; Bray, F. Global Cancer Statistics 2020: GLOBOCAN Estimates of Incidence and Mortality Worldwide for 36 Cancers in 185 Countries. *Ca-Cancer J. Clin.* **2021**, *71*, 209−249.

(2) Bera, H.; Abbasi, Y. F.; Lee Ping, L.; Marbaniang, D.; Mazumder, B.; Kumar, P.; Tambe, P.; Gajbhiye, V.; Cun, D.; Yang, M. Erlotinib-loaded carboxymethyl temarind gum semi-interpenetrating nanocomposites. *Carbohydr. Polym.* **2020**, *230*, No. 115664.

(3) Liu, R.; Yu, M.; Yang, X.; Umeshappa, C. S.; Hu, C.; Yu, W.; Qin, L.; Huang, Y.; Gao, H. Linear Chimeric Triblock Molecules Self-Assembled Micelles with Controllably Transformable Property to Enhance Tumor Retention for Chemo-Photodynamic Therapy of Breast Cancer. *Adv. Funct. Mater.* **2019**, *29*, 1808462.

(4) Tian, X.; Bera, H.; Guo, X.; Xu, R.; Sun, J.; He, Z.; Cun, D.; Yang, M. Pulmonary Delivery of Reactive Oxygen Species/Glutathione-Responsive Paclitaxel Dimeric Nanoparticles Improved Therapeutic Indices against Metastatic Lung Cancer. *ACS Appl. Mater. Interfaces* **2021**, 56858.

(5) Yerlikaya, F.; Ozgen, A.; Vural, I.; Güven, O.; Karaagaoglu, E.; Khan, M. A.; Capan, Y. Development and Evaluation of Paclitaxel Nanoparticles Using a Quality-by-Design Approach. *J. Pharm. Sci.* **2013**, *102*, 3748.

(6) Hu, J.; Yuan, X.; Wang, F.; Gao, H.; Liu, X.; Zhang, W. The Progress and Perspective of Strategies to Improve Tumor Penetration of Nanomedicines. *Chin. Chem. Lett.* **2021**, *32*, 1341−1347.

(7) Sun, J.; Liu, Y.; Chen, Y.; Zhao, W.; Zhai, Q.; Rathod, S.; Huang, Y.; Tang, S.; Kwon, Y. T.; Fernandez, C.; Venkataramanan, R.; Li, S. Doxorubicin Delivered by a Redox-Responsive Dasatinib-containing Polymeric Prodrug Carrier for Combination Therapy. *J. Controlled Release* **2017**, *258*, 43−55.

(8) Liu, R.; Luo, C.; Pang, Z.; Zhang, J.; Ruan, S.; Wu, M.; Wang, L.; Sun, T.; Li, N.; Han, L.; Shi, J.; Huang, Y.; Guo, W.; Peng, S.; Zhou, W.; Gao, H. Advances of Nanoparticles as Drug Delivery Systems for Disease Diagnosis and Treatment. *Chin. Chem. Lett.* **2023**, *34*, 107518.

(9) Zhao, D.; Zhang, H.; Yang, S.; He, W.; Luan, Y. Redox-sensitive mPEG-SS-PTX/TPGS mixed Micelles: An Efficient Drug Delivery System for Overcoming Multidrug Resistance. *Int. J. Pharm.* **2016**, *515*, 281.

(10) Chen, Z.; He, N.; Chen, M.; Zhao, L.; Li, X. Tunable Conjugation Densities of Camptothecin on Hyaluronic Acid for Tumor Targeting and Reduction-triggered Release. *Acta Biomater.* **2016**, *43*, 195−207.

(11) Bera, H.; Abosheasha, M. A.; Ito, Y.; Ueda, M. Etherified Pullulan-polyethylenimine based Nanoscaffolds Improved Chemosensitivity of Erlotinib on Hypoxic Cancer Cells. *Carbohydr. Polym.* **2021**, *271*, No. 118441.

(12) Zhang, A.; Li, A.; Zhao, W.; Yan, G.; Liu, B.; Liu, M.; Li, M.; Huo, B.; Liu, J. An Efficient and Self-guided Chemo-photothermal Drug Loading System Based on Copolymer and Transferrin Decorated MoS2 Nanodots for Dually Controlled Drug Release. *Chem. Eng. J.* **2018**, *342*, 120−132.

(13) Upadhyay, P.; Sarker, S.; Ghosh, A.; Gupta, P.; Das, S.; Ahir, M.; Bhattacharya, S.; Chattopadhyay, S.; Ghosh, S.; Adhikary, A. Transferrin-decorated Thymoquinone-loaded PEG-PLGA Nanopar-

ticles Exhibit Anticarcinogenic Effect in Non-small Cell Lung Carcinoma via the Modulation of miR-34a and miR-16. *Biomater. Sci.* **2019**, *7*, 4325−4344.
(14) Huang, L.; Chaurasiya, B.; Wu, D.; Wang, H.; Du, Y.; Tu, J.; Webster, T. J.; Sun, C. Reversibly Disulfide-crosslinked Pullulan Nanoparticles for Dual-targeted and Bio-triggered Anti-tumor Liver Drug Delivery. *Nanomed.: Nanotechnol., Biol. Med.* **2018**, *14*, 1005.
(15) Jana, P.; Mitra, D.; Selvaraj, T. K. R.; Gnanamani, A.; Kundu, P. P. Preparation of Guar Gum Scaffold Film Grafted with Ethylenediamine and Fish Scale Collagen, Cross-linked with Ceftazidime for Wound Healing Application. *Carbohydr. Polym.* **2016**, *153*, 573.
(16) Zhang, J.; Wang, L.; Fai Chan, H.; Xie, W.; Chen, S.; He, C.; Wang, Y.; Chen, M. Co-delivery of Paclitaxel and Tetrandrine via iRGD Peptide Conjugated Lipid-polymer Hybrid Nanoparticles Overcome Multidrug Resistance in Cancer Cells. *Sci. Rep.* **2017**, *7*, 46057.
(17) Kulkarni, A.; Rao, P.; Natarajan, S.; Goldman, A.; Sabbisetti, V. S.; Khater, Y.; Korimerla, N.; Chandrasekar, V.; Mashelkar, R. A.; Sengupta, S. Reporter Nanoparticle that Monitors its Anticancer Efficacy in Real Time. *Proc. Natl. Acad. Sci. U. S. A.* **2016**, *113*, E2104.
(18) Stella, B.; Arpicco, S.; Peracchia, M. T.; Desmaële, D.; Hoebeke, J.; Renoir, M.; D'Angelo, J.; Cattel, L.; Couvreur, P. Design of Folic Acid-conjugated Nanoparticles for Drug Targeting. *J. Pharm. Sci.* **2000**, *89*, 1452−1464.
(19) Gericke, M.; Schulze, P.; Heinze, T. Nanoparticles Based on Hydrophobic Polysaccharide Derivatives—Formation Principles, Characterization Techniques, and Biomedical Applications. *Macromol. Biosci.* **2020**, *20*, 1900415.
(20) Liu, K.; Dai, L.; Li, C.; Liu, J.; Wang, L.; Lei, J. Self-assembled Targeted Nanoparticles Based on Transferrin-modified Eight-arm-polyethylene Glycol−dihydroartemisinin Conjugate. *Sci. Rep.* **2016**, *6*, 29461.
(21) Mulik, R. S.; Mönkkönen, J.; Juvonen, R. O.; Mahadik, K. R.; Paradkar, A. R. Transferrin Mediated Solid Lipid Nanoparticles Containing Curcumin: Enhanced in Vitro Anticancer Activity by Induction of Apoptosis. *Int. J. Pharm.* **2010**, *398*, 190−203.
(22) Salvati, A.; Pitek, A. S.; Monopoli, M. P.; Prapainop, K.; Bombelli, F. B.; Hristov, D. R.; Kelly, P. M.; Åberg, C.; Mahon, E.; Dawson, K. A. Transferrin-functionalized Nanoparticles Lose their Targeting Capabilities when a Biomolecule Corona Adsorbs on the Surface. *Nat. Nanotechnol.* **2013**, *8*, 137−143.
(23) Sun, B.; Luo, C.; Yu, H.; Zhang, X.; Chen, Q.; Yang, W.; Wang, M.; Kan, Q.; Zhang, H.; Wang, Y.; He, Z.; Sun, J. Disulfide Bond-Driven Oxidation- and Reduction-Responsive Prodrug Nanoassemblies for Cancer Therapy. *Nano Lett.* **2018**, *18*, 3643−3650.
(24) Pei, Q.; Hu, X.; Liu, S.; Li, Y.; Xie, Z.; Jing, X. Paclitaxel Dimers Assembling Nanomedicines for Treatment of Cervix Carcinoma. *J. Controlled Release* **2017**, *254*, 23−33.
(25) Han, X.; Chen, J.; Jiang, M.; Zhang, N.; Na, K.; Luo, C.; Zhang, R.; Sun, M.; Lin, G.; Zhang, R.; Ma, Y.; Liu, D.; Wang, Y. Paclitaxel-Paclitaxel Prodrug Nanoassembly as a Versatile Nanoplatform for Combinational Cancer Therapy. *ACS Appl. Mater. Interfaces* **2016**, *8*, 33506−33513.
(26) Sun, B.; Luo, C.; Zhang, X.; Guo, M.; Sun, M.; Yu, H.; Chen, Q.; Yang, W.; Wang, M.; Zuo, S.; Chen, P.; Kan, Q.; Zhang, H.; Wang, Y.; He, Z.; Sun, J. Probing the Impact of Sulfur/Selenium/Carbon Linkages on Prodrug Nanoassemblies for Cancer Therapy. *Nat. Commun.* **2019**, *10*, 3211.
(27) Luo, C.; Sun, J.; Sun, B.; Liu, D.; Miao, L.; Goodwin, T. J.; Huang, L.; He, Z. Facile Fabrication of Tumor Redox-Sensitive Nanoassemblies of Small-Molecule Oleate Prodrug as Potent Chemotherapeutic Nanomedicine. *Small* **2016**, *12*, 6353−6362.
(28) Huang, X.; Chisholm, J.; Zhuang, J.; Xiao, Y.; Duncan, G.; Chen, X.; Suk, J. S.; Hanes, J. Protein Nanocages that Penetrate Airway Mucus and Tumor Tissue. *Proc. Natl. Acad. Sci. U. S. A.* **2017**, *114*, E6595.
(29) Gan, C. W.; Feng, S.-S. Transferrin-Conjugated Nanoparticles of Poly(Lactide)-D-_-Tocopheryl Polyethylene Glycol Succinate Diblock Copolymer for Targeted Drug Delivery across the Blood−Brain Barrier. *Biomaterials* **2010**, *31*, 7748−7757.
(30) An, L.; Zhang, P.; Shen, W.; Yi, X.; Yin, W.; Jiang, R.; Xiao, C. A Sulfur Dioxide Polymer Prodrug Showing Combined Effect with Doxorubicin in Combating Subcutaneous and Metastatic Melanoma. *Bioact. Mater.* **2021**, *6*, 1365−1374.
(31) Liang, M.; Chen, X.; Wang, L.; Qin, L.; Wang, H.; Sun, Z.; Zhao, W.; Geng, B. Cancer-Derived Exosomal TRIM59 Regulates Macrophage NLRP3 Inflammasome Activation to Promote Lung Cancer Progression. *J. Exp. Clin. Cancer Res.* **2020**, *39*, 176.
(32) Wang, K.; Ye, H.; Zhang, X.; Wang, X.; Yang, B.; Luo, C.; Zhao, Z.; Zhao, J.; Lu, Q.; Zhang, H.; Kan, Q.; Wang, Y.; He, Z.; Sun, J. An Exosome-like Programmable-Bioactivating Paclitaxel Prodrug Nanoplatform for Enhanced Breast Cancer Metastasis Inhibition. *Biomaterials* **2020**, *257*, No. 120224.
(33) Wang, Z.; Yu, Y.; Dai, W.; Cui, J.; Wu, H.; Yuan, L.; Zhang, H.; Wang, X.; Wang, J.; Zhang, X.; Zhang, Q. A Specific Peptide Ligand-modified Lipid Nanoparticle Carrier for the Inhibition of Tumor Metastasis Growth. *Biomaterials* **2013**, *34*, 756−764.
(34) Zhang, Y.; Li, T.; Hu, Y.; Chen, J.; He, Y.; Gao, X.; Zhang, Y. Co-delivery of Doxorubicin and Curcumin via cRGD-peptide Modified PEG-PLA Self-Assembly Nanomicelles for Lung Cancer Therapy. *Chin. Chem. Lett.* **2022**, *33*, 2507−2511.
(35) Gammella, E.; Lomoriello, I. S.; Conte, A.; Freddi, S.; Alberghini, A.; Poli, M.; Sigismund, S.; Cairo, G.; Recalcati, S. Unconventional Endocytosis and Trafficking of Transferrin Receptor Induced by Iron. *Mol. Biol. Cell* **2021**, *32*, 98−108.
(36) Richard, D. K.; Gilbert, A.; JOS, V. R.; JOE, B. H.; Kenneth, R. B. Unconventional Endocytosis and Trafficking of Transferrin Receptor Induced by Iron. *Proc. Natl. Acad. Sci. U. S. A.* **1983**, *80*, 2263−2266.
(37) Kang, H.; Guan, L.; An, K.; Tian, D. Preparation and Physicochemical Properties of Konjac Glucomannan Ibuprofen Ester as a Polysaccharide-drug Conjugate. *J. Macromol. Sci., Part A: Pure Appl.Chem.* **2021**, *58*, 32−43.
(38) Italia, J. L.; Sharp, A.; Carter, K. C.; Warn, P.; Kumar, M. N. V. R. Peroral Amphotericin B Polymer Nanoparticles Lead to Comparable or Superior In Vivo Antifungal Activity to That of Intravenous Ambisome® or Fungizone™. *PLoS One* **2011**, *6*, No. e25744.
(39) Mateovic, T.; Kriznar, B.; Bogataj, M.; Mrhar, A. The Influence of Stirring Rate on Biopharmaceutical Properties of Eudragit RS Microspheres. *J. Microencapsulation* **2002**, *19*, 29−36.
(40) Şahinoğlu, E.; Uslu, T. Effects of Various Parameters on Ultrasonic Comminution of Coal in Water Media. *Fuel Process. Technol.* **2015**, *137*, 48−54.
(41) Zhao, D.; Wu, J.; Li, C.; Zhang, H.; Li, Z.; Luan, Y. Precise Ratiometric Loading of PTX and DOX based on Redox-Sensitive Mixed Micelles for Cancer Therapy. *Colloids Surf., B* **2017**, *155*, 51−60.
(42) Pinheiro, R.; Granja, A.; Loureiro, J.; Pereira, M. C.; Pinheiro, M.; Neves, A. R.; Reis, S. Quercetin Lipid Nanoparticles Functionalized with Transferrin for Alzheimer's Disease. *Eur. J. Pharm. Sci.* **2020**, *148*, No. 105314.
(43) Martens, U.; Böttcher, D.; Talbot, D.; Bornscheuer, U.; Abou-Hassan, A.; Delcea, M. Maghemite Nanoparticles Stabilize the Protein Corona Formed with Transferrin Presenting Different Iron-saturation Levels. *Nanoscale* **2019**, *11*, 16063−16070.
(44) Calmettes, C.; Alcantara, J.; Yu, R.-H.; Schryvers, A. B.; Moraes, T. F. The Structural Basis of Transferrin Sequestration by Transferrin-binding Protein B. *Nat. Struct. Mol. Biol.* **2012**, *19*, 358−360.
(45) Li, J.; Huo, M.; Wang, J.; Zhou, J.; Mohammad, J. M.; Zhang, Y.; Zhu, Q.; Waddad, A. Y.; Zhang, Q. Redox-Sensitive Micelles Self-Assembled from Amphiphilic Hyaluronic Acid-Deoxycholic Acid Conjugates for Targeted Intracellular Delivery of Paclitaxel. *Biomaterials* **2012**, *33*, 2310−2320.
(46) Chen, H.; Liu, Z.; Wei, B.; Huang, J.; You, X.; Zhang, J.; Yuan, Z.; Tang, Z.; Guo, Z.; Wu, J. Redox Responsive Nanoparticle

Encapsulating Black Phosphorus Quantum Dots for Cancer Theranostics. *Bioact. Mater.* **2021**, *6*, 655−665.
(47) Calzolari, A.; Oliviero, I.; Deaglio, S.; Mariani, G.; Biffoni, M.; Sposi, N. M.; Malavasi, F.; Peschle, C.; Testa, U. Transferrin Receptor 2 is Frequently Expressed in Human Cancer Cell Lines. *Blood Cells, Mol., Dis.* **2007**, *39*, 82−91.
(48) Sawant, R. R.; Jhaveri, A. M.; Koshkaryev, A.; Zhu, L.; Qureshi, F.; Torchilin, V. P. Targeted Transferrin-Modified Polymeric Micelles: Enhanced Efficacy in Vitro and in Vivo in Ovarian Carcinoma. *Mol. Pharmaceutics* **2014**, *11*, 375−381.
(49) Gustafson, H. H.; Holt-Casper, D.; Grainger, D. W.; Ghandehari, H. Nanoparticle Uptake: The Phagocyte Problem. *Nano Today* **2015**, *10*, 487−510.
(50) Tamura, R.; Uemoto, S.; Tabata, Y. Augmented Liver Targeting of Exosomes by Surface Modification with Cationized Pullulan. *Acta Biomater.* **2017**, *57*, 274−284.
(51) Cui, Y.; Xu, Q.; Chow, P. K.-H.; Wang, D.; Wang, C.-H. Transferrin-conjugated Magnetic Silica PLGA Nanoparticles Loaded with Doxorubicin and Paclitaxel for Brain Glioma Treatment. *Biomaterials* **2013**, *34*, 8511−8520.
(52) Mukherjee, S.; Kotcherlakota, R.; Haque, S.; Bhattacharya, D.; Kumar, J. M.; Chakravarty, S.; Patra, C. R. Improved Delivery of Doxorubicin Using Rationally Designed PEGylated Platinum Nanoparticles for the Treatment of Melanoma. *Mater. Sci. Eng., C* **2020**, *108*, No. 110375.

https://doi.org/10.1021/acsami.2c18422
ACS Appl. Mater. Interfaces 2023, 15, 4441−4457